Programming shape-morphing electroactive polymers through multi-material topology optimisation

Rogelio Ortigosa[†*], Jesús Martínez-Frutos[†], Antonio J. Gil[‡]

[†] *Technical University of Cartagena, Campus Muralla del Mar, 30202, Cartagena (Murcia), Spain*
[‡] *Zienkiewicz Centre for Computational Engineering, Faculty of Science and Engineering Swansea University, Bay Campus, SA1 8EN, United Kingdom*

Abstract

This paper presents a novel engineering strategy for the design of Dielectric Elastomer (DE) based actuators, capable of attaining complex electrically induced shape morphing configurations. In this approach, a multilayered DE prototype, interleaved with compliant electrodes spreading across the entire faces of the DE, is considered. Careful combination of several DE materials, characterised by different material properties within each of the multiple layers of the device, is pursued. The resulting layout permits the generation of a heterogenous electric field within the device due to the spatial variation of the material properties within the layers and across them. An in-silico or computational approach has been developed in order to facilitate the design of new prototypes capable of displaying predefined electrically induced target configurations. Key features of this framework are: (i) use of a standard two-field Finite Element implementation of the underlying partial differential equations in reversible nonlinear electromechanics, where the unknown fields ot the resulting discrete problem are displacements and the scalar electric potential; (ii) introduction of a novel phase-field driven multi-material topology optimisation framework allowing for the consideration of several DE materials with different material properties, favouring the development of heterogeneous electric fields within the prototype. This novel multi-material framework permits, for the first time, the consideration of an arbitrary number of different N DE materials, by means of the introduction of $N-1$ phase-field functions, evolving independently over the different layers across the thickness of the device through $N-1$ Allen-Cahn type evolution equations per layer. A comprehensive series of numerical examples is analysed, with the aim of exploring the capability of the proposed methodology to propose efficient optimal designs. Specifically, the topology optimisation algorithm determines the topology of regions where different DE materials must be conveniently placed in order to attain complex electrically induced configurations.

Keywords: Multi-material; Topology Optimisation; Dielectric Elastomer; Finite Elements; Phase-Field

1. Introduction

Dielectric Elastomers (DEs) [1, 2, 3, 4, 5] are a special type of Electro Active Polymers (EAPs), a sub-group within smart or multi-functional materials. DEs, which are extremely soft elastomeric materials, are typically sandwiched by a pair of oppositely charged electrodes placed across their thin thickness. As a result, Coulomb forces develop between the electrodes, inducing thinning across the thickness of the DE. Then, its near-incompressible nature leads to an in-plane expansion, ultimately yielding large area expansions [3, 6, 7]. Consequently, the inherent capability of DEs to exhibit large electrically induced deformations, resulting from the interplay between their mechanical and electrical physics, in conjunction with their low stiffness and bio-mimetic dexterous features, have led to their identification as ideal candidates in the field of soft robotics [8, 9, 10, 11]. Nonetheless, the potential of DEs is not restricted to the field of electrically induced actuation, as they have been successfully used as Braille displays, deformable lenses, haptic devices and energy generators, to name but a few [12].

For the case of nearly flat DE designs, the electric field remains mostly uniform everywhere within the homogeneous (material properties do not vary spatially) elastomeric material. This reflects in the homogeneity of the electrically induced deformations (prior to the development of wrinkles triggered by boundary conditions [6, 13, 14]). Relatively more complex eletrically induced bending deformations have been achieve through the attachment of passive elastomeric layers [15, 16]. However, more advanced actuation configurations are still hindered by either: (i) the relatively homogeneous electric field distribution across the DE device; (ii) the homogeneous material properties of the DE across the device. With that in mind, very recent experimental research at Clarke

*Corresponding author
Email addresses: rogelio.ortigosa@upct.es (Rogelio Ortigosa[†]), jesus.martinez@upct.es (Jesús Martínez-Frutos[†]), a.j.gil@swansea.ac.uk (Antonio J. Gil[‡])

Lab (Harvard) [17, 18] has pursued the introduction of new technologies capable of generating either highly inhomogeneous electric field distributions or heterogeneous material properties with the aim of attaining complex electrically induced shape morphing configurations. Specifically, two different types of engineering solutions were found in order to accomplish that objective. In the first [17], a multi-layer layout comprising a set of elastomeric DE layers intercalating compliant electrodes (of alternating polarity) with different shapes was pursued. The exploration of various electrode meso-architectures enabled the attainability of sophisticated electrically induced configurations through the generation of highly heterogeneous electric fields within the elastomeric layers. In a second approach, Clarke et. al. [18] proposed a layout where an active layer of elastomer (subjected to a voltage gradient across its thickness) was attached to passive material on one or both of its sides in contact with the electrodes, acting as stiffeners or as a smart exoskeleton. Although the electric field generated within the active DE layer through this mechanism is practically uniform, the material heterogeneity induced by the combination of the active material and the conveniently placed passive material led to an anisotropic behaviour of the overall device. This was crucial to allow for the attainability of complex electrically induced shape morphing configurations.

Figure 1 demonstrates that the same electrically induced deformation can be obtained by both approaches. The results shown in Figure 1 are taken from References [19, 20]. Therein, the authors of the present paper, inspired by the pioneering experimental work at Clarke Lab (Harvard) [17, 18], decided to explore state-of-the-art topology optimisation techniques with the aim of attaining specific electrically induced target shape morphing configurations through the two mechanisms described, namely: (i) the design of the electro meso-architecture [19] (see Figure 1_a); (ii) the design of the exoskeleton attached to an active DE layer [20] (see Figure 1_b).

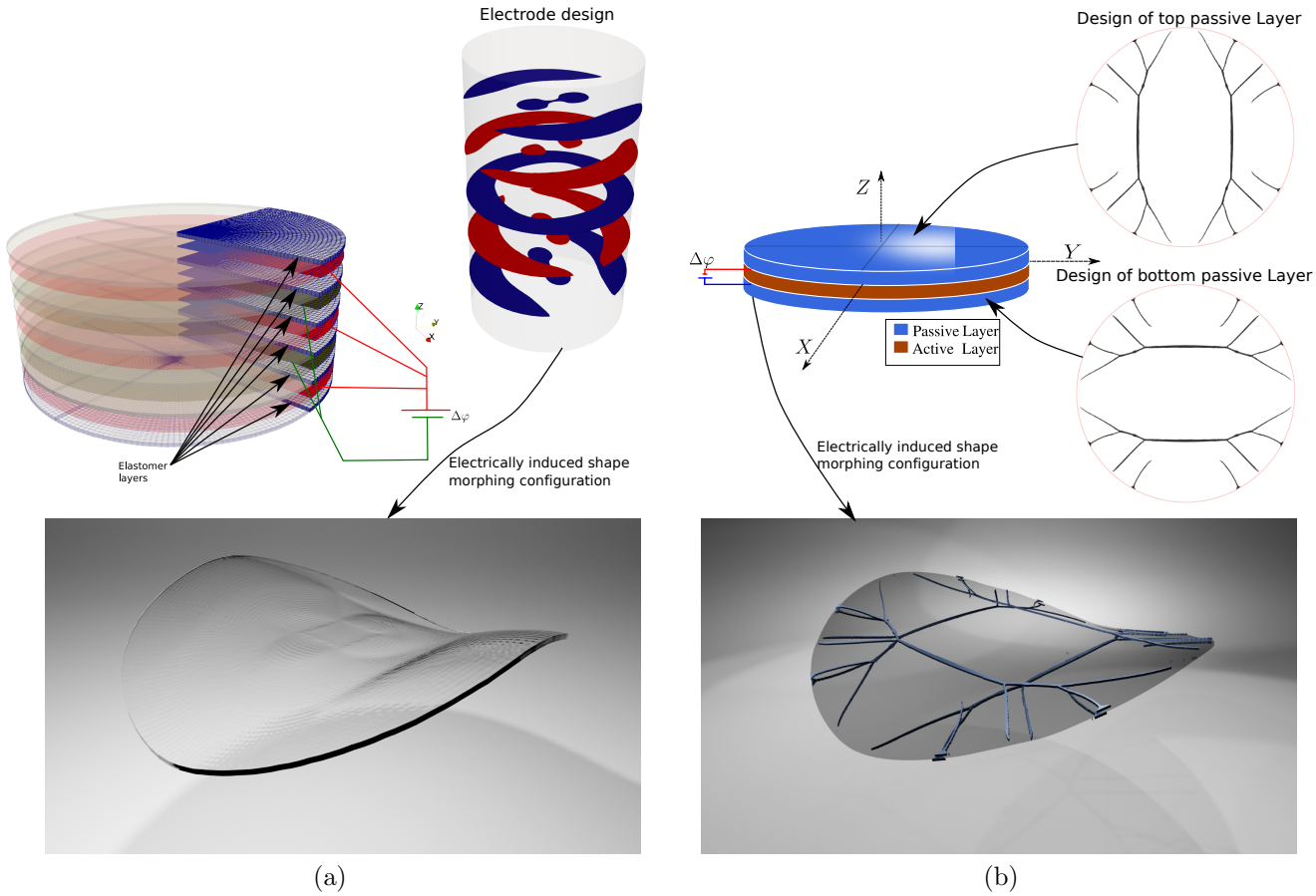

Figure 1: (a) Multilayered structure of circular elastomer sheets interleaved with electrodes with different shapes (red and blue surfaces). The electric field is primarily concentrated in the regions of overlap between the adjacent electrodes, yielding a heterogeneous electric field inside the device, inducing a positive and negative Gaussian curvature upon application of electric potential on the electrodes. Results from [19]. (b) A layer of DE is attached to two layers of carefully designed stiffeners on both sides. The resulting exoskeleton induces positive and negative Gaussian curvatures upon application of electric potential on the electrodes. Results from [20].

In the present manuscript, a third alternative engineering solution is investigated with the aim of generating complex electrically induced shape morphing configurations. In this new approach, a multilayered DE device, interleaved with compliant electrodes spreading across the entire faces of the DE, is considered. Then, the careful combination of several DE materials with different material properties (multi-material approach) within each of the multiple layers of the device is sought through the application of topology optimisation techniques. This ultimately leads to a heterogenous electric field within the device due to the spatial variation of the material properties within the layers and across them. In order to achieve the design objective described in the new

approach proposed, we advocate for a specific methodology which relies on two key ingredients: (i) an accurate Finite Element framework for numerical simulation in the context of nonlinear electromechanics; (ii) the application of cutting edge topology optimisation techniques in nonlinear multi-physics problems. Both features will certainly benefit from subsequent experimental verification of the designs proposed. This is indeed the object of follow up publications were we intend to crystallise the designs proposed through our mathematically-driven strategy into real prototypes for their verification in the lab. However, the multi-disciplinarity required to cover the three aspects mentioned demands to moderate our ambitions and to focus initially on the two aspects which are within our current area of expertise, addressing the experimental facet at due time relying on the valuable aid of experts in the field. Nonetheless, a review on state-of-the-art additive manufacturing technologies that allow for multi-material printing of active materials, critical to materialise the designs obtained in the present manuscript into real prototypes, can be found in References [21, 22, 23]. Furthermore, a crucial benefit from the proposed topology optimisation-based approach is that it easily enables its generalisation to other types of active materials such as thermo-active and magneto-active materials [24, 25, 26, 27].

With regards to the numerical simulation of DEs, the consideration of two-field variational formulations, where displacements and electric potential are the unknown fields of the problem, represents the most popular choice [28, 29, 30, 31, 32, 33, 32]. In this formulation, the constitutive information of the material is encapsulated in the free energy density. The latter must comply with mathematical and physical conditions. The most well-accepted of these is the Legendre-Hadamard or ellipticity condition [34], which ensures the well-posedness of the underlying system of differential governing equations. A sufficient condition complying with the ellipticity condition is that of polyconvexity [34, 35, 36]. Extension of this condition to the field of nonlinear electromechanics was postulated in Reference [37]. In this paper, however, and without loss of generality, we do not contemplate extreme scenarios beyond the onset of loss of ellipticity. Hence, commonly used free energy densities will be used.

With regards to Topology Optimisation (TO) of smart materials, density-based methods, seem to be the preferred choice. Among these, the Solid Isotropic Material with Penalisation (SIMP) method [38] is the most popular alternative. However, there are other techniques available such as level-set methods [39, 40], phase-field methods [41, 42], topological derivative methods [43] and evolutionary methods [44]. Kang and Wang [45] used the SIMP method for the topology optimisation of piezoelectric ceramics, restricted to small electrically induced deformations. The works in references [46] and [47] apply TO to piezoelectric ceramics and flexoelectric materials. Zhang et. al. also applied TO for the design of piezoelectric sensors for active vibration control. Other works [48, 49, 50, 51] have investigated the simultaneous optimisation of polarisation and layout of piezoelectric ceramics over a fixed host (passive) material, and when the host structure is also included in the optimisation process [52, 53, 54]. Furthermore, the work in [55] carries out the TO of piezoelectric ceramic-based micro-grippers considering geometrical nonlinearities. Some recent works include the TO design of thermo-electric coolers and generators [56, 57, 58]. In addition, the work in [59] explores TO of DEs seeking to maximise electrically induced rotations of a rotary device. The work in [60] explored TO of DEs for the design of wide tunable band gaps. Through the use of the SIMP method, the authors in [61, 62] applied TO for the design of DE materials for actuation purposes. In addition, as already mentioned above, [20] explored density-based topology optimisation for the design of the exoskeleton attached to a film of DE with the aim of attaining specific electrically induced target configurations upon application of electric voltage on the electrodes attached to the DE film. Reference [19], also described above, made use of phase-field driven topology optimisation for the careful design of electrode meso-architecture in order to yield specific electrically induced target configurations.

The layout of this paper is as follows: Section 2 introduces the governing equations in nonlinear electromechanics and the basic notions for the definition of invariant-based constitutive models in this context. Section 3 describes the main ingredients of the multi-material phase-field driven topology optimisation approach proposed. The Section concludes with an algorithmic flowchart that summarises the proposed computational approach. Section 4 presents a series of numerical examples in order to demonstrate the robustness of the proposed methodology and present various designs for complex three dimensional actuation modes. Section 5 provides some concluding remarks and future lines of research. Finally, Appendix A summarises the Finite Element spatial discretisation technique.

2. Governing equations in nonlinear reversible electro-mechanics

A brief description of the differential governing equations will be carried out in this section. In addition, a succinct overview on the definition of constitutive models in the context of nonlinear electromechanics will be given, prior to the definition of suitable variational principles in this context.

2.1. Differential governing equations in nonlinear electromechanics

Let $\mathcal{B}_0 \subset \mathbb{R}^3$ represent the reference configuration of a DE, with unit outward normal $\boldsymbol{N}$ (see Figure 1). After the motion, the DE occupies a deformed configuration $\mathcal{B} \subset \mathbb{R}^3$ with boundary $\partial\mathcal{B}$ and unit outward normal $\boldsymbol{n}$. The deformation mapping $\boldsymbol{\phi}$ relates material particles $\boldsymbol{X} \in \mathcal{B}_0$ to the deformed configuration $\boldsymbol{x} \in \mathcal{B}$ according to

$\boldsymbol{x} = \boldsymbol{\phi}(\boldsymbol{X})$, and permits to introduce the deformation gradient tensor $\boldsymbol{F}$ [63], the co-factor $\boldsymbol{H}$ and its Jacobian J as

$$\boldsymbol{F} = \boldsymbol{\nabla}_0 \boldsymbol{\phi} := \partial_{\boldsymbol{X}} \boldsymbol{\phi}; \qquad \boldsymbol{H} = \frac{1}{2} \boldsymbol{F} \times \boldsymbol{F}; \qquad J = \frac{1}{3} \boldsymbol{H} : \boldsymbol{F}, \tag{1}$$

where $\times$ represents a tensor cross product operation [64, 65] between second order tensors defined as $(\boldsymbol{A} \times \boldsymbol{B})_{iI} = \mathcal{E}_{ijk} \mathcal{E}_{IJK} A_{jJ} B_{kK}$, $\forall \boldsymbol{A}, \boldsymbol{B} \in \mathbb{R}^{3\times3}$, where $\mathcal{E}_{ijk}$ (or $\mathcal{E}_{IJK}$) symbolises the third-order alternating tensor components and the use of repeated indices implies summation[1].

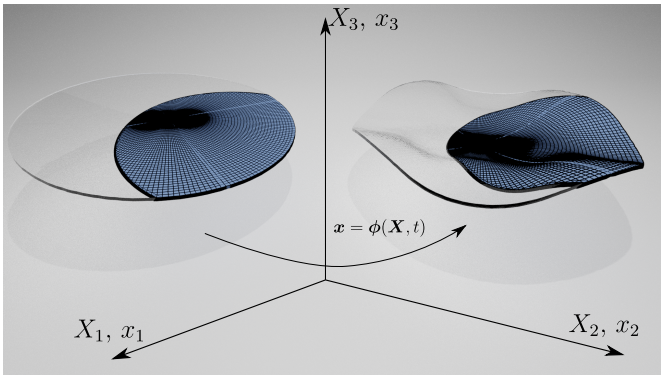

Figure 2: Deformation mapping $\boldsymbol{\phi}(\boldsymbol{X})$ for the DE in material configuration (left) and deformed configuration (right).

In the absence of inertia effects, the mechanical response of the DE is represented by

$$\boldsymbol{F} = \boldsymbol{\nabla}_0 \boldsymbol{\phi}; \qquad \text{in } \mathcal{B}_0; \tag{2a}$$
$$\mathrm{DIV} \boldsymbol{P} + \boldsymbol{f}_0 = \boldsymbol{0}; \qquad \text{in } \mathcal{B}_0; \tag{2b}$$
$$\boldsymbol{P}\boldsymbol{N} = \boldsymbol{t}_0; \qquad \text{on } \partial_{\boldsymbol{t}}\mathcal{B}_0; \tag{2c}$$
$$\boldsymbol{\phi} = \bar{\boldsymbol{\phi}}^b; \qquad \text{on } \partial_{\boldsymbol{\phi}}\mathcal{B}_0, \tag{2d}$$

where (2a) represents the kinematic compatibility equation and (2b) the quasi-static version of the conservation of linear momentum in a Lagrangian setting. In above equations, $\boldsymbol{f}_0$ represents a body force per unit undeformed volume, $\boldsymbol{P}$ is the first Piola-Kirchhoff stress tensor, $\boldsymbol{t}_0$ is the external traction vector per unit undeformed area $\partial_{\boldsymbol{t}}\mathcal{B}_0 \subset \partial\mathcal{B}_0$ and $\bar{\boldsymbol{\phi}}^b$ the Dirichlet type boundary condition on $\partial_{\boldsymbol{\phi}}\mathcal{B}_0 \subset \partial\mathcal{B}_0$, with $\partial_{\boldsymbol{t}}\mathcal{B}_0 \cup \partial_{\boldsymbol{\phi}}\mathcal{B}_0 = \partial\mathcal{B}_0$ and $\partial_{\boldsymbol{t}}\mathcal{B}_0 \cap \partial_{\boldsymbol{\phi}}\mathcal{B}_0 = \emptyset$.

Similarly, and in the absence of magnetic effects, the electrical response of the DE is represented by

$$\boldsymbol{E}_0 = -\boldsymbol{\nabla}_0 \varphi; \qquad \text{in } \mathcal{B}_0; \tag{3a}$$
$$\mathrm{DIV} \boldsymbol{D}_0 - \rho_0 = 0; \qquad \text{in } \mathcal{B}_0; \tag{3b}$$
$$\boldsymbol{D}_0 \cdot \boldsymbol{N} = -\omega_0; \qquad \text{on } \partial_\omega\mathcal{B}_0; \tag{3c}$$
$$\varphi = \bar{\varphi}^b; \qquad \text{on } \partial_\varphi\mathcal{B}_0, \tag{3d}$$

where (3a) and (3b) denote the quasi-static version of the Gauss' and Faraday's laws in a Lagrangian setting. In above equations, φ represents an scalar electric potential, $\boldsymbol{E}_0$ denotes the material electric field, $\boldsymbol{D}_0$ the material electric displacement, ρ_0 represents an electric charge per unit of undeformed volume, ω_0 an electric charge per unit of undeformed area $\partial_\omega\mathcal{B}_0 \subset \partial\mathcal{B}_0$ and $\bar{\varphi}^b$ the electric potential applied on electrodes, positioned on $\partial_\varphi\mathcal{B}_0 \subset \partial\mathcal{B}_0$, such that $\partial_\omega\mathcal{B}_0 \cup \partial_\varphi\mathcal{B}_0 = \partial\mathcal{B}_0$ and $\partial_\omega\mathcal{B}_0 \cap \partial_\varphi\mathcal{B}_0 = \emptyset$.

2.2. Constitutive equations in reversible nonlinear electromechanics

A constitutive law is required in order to relate the first $\boldsymbol{P}$ and $\boldsymbol{D}_0$ with the quantities $\boldsymbol{F}$ and $\boldsymbol{E}_0$ in (2) and (3), namely $\boldsymbol{P} = \boldsymbol{P}(\boldsymbol{F}, \boldsymbol{E}_0)$ and $\boldsymbol{D}_0 = \boldsymbol{D}_0(\boldsymbol{F}, \boldsymbol{E}_0)$. For the case of reversible nonlinear electromechanics, this is done through the definition of the free energy density function per unit undeformed volume $\mathcal{B}_0$ [28, 66, 67, 68, 69], denoted as $\Psi = \Psi(\boldsymbol{F}, \boldsymbol{E}_0)$. From the latter, the first Piola-Kirchhoff stress tensor $\boldsymbol{P}$ and the electric displacement field $\boldsymbol{D}_0$ emerge as

$$\boldsymbol{P}(\boldsymbol{F}, \boldsymbol{E}_0) = \partial_{\boldsymbol{F}} \Psi(\boldsymbol{F}, \boldsymbol{E}_0); \qquad \boldsymbol{D}_0(\boldsymbol{F}, \boldsymbol{E}_0) = -\partial_{\boldsymbol{E}_0} \Psi(\boldsymbol{F}, \boldsymbol{E}_0). \tag{4}$$

[1] In addition, throughout the paper, the symbol $(\cdot)$ indicates the scalar product or contraction of a single index $\boldsymbol{a} \cdot \boldsymbol{b} = a_i b_i$; the symbol $(:)$, double contraction of two indices $\boldsymbol{A} : \boldsymbol{B} = A_{ij} B_{ij}$; and the symbol $(\otimes)$, the outer or dyadic product $(\boldsymbol{a} \otimes \boldsymbol{b})_{ij} = a_i b_j$.

Furthermore, the so-called constitutive tensors emerge as,

$$\boldsymbol{\mathcal{C}}(\boldsymbol{F},\boldsymbol{E}_0)=\partial^2_{\boldsymbol{FF}}\Psi(\boldsymbol{F},\boldsymbol{E}_0);\qquad \boldsymbol{\mathcal{P}}(\boldsymbol{F},\boldsymbol{E}_0)=-\partial^2_{\boldsymbol{E}_0\boldsymbol{F}}\Psi(\boldsymbol{F},\boldsymbol{E}_0);\qquad \boldsymbol{\varepsilon}(\boldsymbol{F},\boldsymbol{E}_0)=-\partial^2_{\boldsymbol{E}_0\boldsymbol{E}_0}\Psi(\boldsymbol{F},\boldsymbol{E}_0). \tag{5}$$

where $\{\boldsymbol{\mathcal{C}},\boldsymbol{\mathcal{P}},\boldsymbol{\theta}\}$ correspond with the fourth order elasticity tensor, the third order piezoelectric tensor and the second order dielectric tensor, respectively. Usually, an additive split of the free energy density is adopted between a purely mechanical contribution $\Psi_m(\boldsymbol{F})$ and an additional contribution encapsulating the electromechanical coupling, denoted as $\Psi_{em}(\boldsymbol{F},\boldsymbol{E}_0)$, i.e

$$\Psi(\boldsymbol{F},\boldsymbol{E}_0)=\Psi_m(\boldsymbol{F})+\Psi_{em}(\boldsymbol{F},\boldsymbol{E}_0). \tag{6}$$

The Mooney-Rivlin model [70] is a typical example of the purely mechanical contribution $\Psi_m=\Psi_m^{MR}$, and it is defined as

$$\Psi_m^{MR}(\boldsymbol{F}):=\frac{\mu_1}{2}\left(II_{\boldsymbol{F}}-3\right)+\frac{\mu_2}{2}\left(II_{\boldsymbol{H}}-3\right)+f(J);\qquad f(J)=-\left(\mu_1+2\mu_2\right)\ln(J)+\frac{\lambda}{2}\left(J-1\right)^2, \tag{7}$$

with $II_{\boldsymbol{A}}=\boldsymbol{A}:\boldsymbol{A}$ and $\{\mu_1,\mu_2,\lambda\}$ can be related to the Young's modulus E and Poisson ratio ν in the origin, namely when $\boldsymbol{F}=\boldsymbol{I}$ (with $\boldsymbol{I}$ the second order identity tensor) and $\boldsymbol{E}_0=\boldsymbol{0}$, as

$$\mu_1+\mu_2=\frac{E}{2(1+\nu)};\qquad \lambda+2\mu_2=\frac{E\nu}{(1+\nu)(1-2\nu)}. \tag{8}$$

The free energy can be additively decomposed into a polarization term $\Psi^P_{em}(\boldsymbol{F},\boldsymbol{E}_0)$ and a Maxwell term $\Psi^M_{em}(\boldsymbol{F},\boldsymbol{E}_0)$. For the case when the DE is immersed in vacuum, and under the consideration of a simple ideal DE model, both contributions are defined as

$$\Psi^P_{em}(\boldsymbol{F},\boldsymbol{E}_0)=-\frac{\chi\varepsilon_0}{2J}II_{\boldsymbol{HE}_0};\qquad \Psi^M_{em}(\boldsymbol{F},\boldsymbol{E}_0)=-\frac{\varepsilon_0}{2J}II_{\boldsymbol{HE}_0};\qquad II_{\boldsymbol{HE}_0}=\boldsymbol{HE}_0\cdot\boldsymbol{HE}_0, \tag{9}$$

where ε_0 represents the electric permittivity of vacuum, being $\varepsilon_0=8.854\times10^{-12}\,\mathrm{Fm}^{-1}$, and χ, the electric susceptibility. Therefore, for this specific case, the free energy $\Psi_{em}(\boldsymbol{F},\boldsymbol{E}_0)$ can be written as

$$\Psi_{em}(\boldsymbol{F},\boldsymbol{E}_0)=-\frac{\varepsilon_r\varepsilon_0}{2J}II_{\boldsymbol{HE}_0};\qquad \varepsilon_r=1+\chi, \tag{10}$$

where ε_r denotes the relative electric permittivity of the material with respect to that of vacuum ε_0.

Remark. *The electromechanical contribution Ψ_{em} in* (10) *represents one of the simplest models to describe the coupled nature of the elastomer. Other more advanced and realistic models may consider the nonlinear dependence of the electric permittivity with respect to deformation. The electric permittivity tensor, denoted as $\widetilde{\boldsymbol{\varepsilon}}$, is defined in terms of its material counterpart $\boldsymbol{\varepsilon}$ in* (5) *as*

$$\widetilde{\boldsymbol{\varepsilon}}=J^{-1}\boldsymbol{F}\boldsymbol{\varepsilon}\boldsymbol{F}^T. \tag{11}$$

The spatial permittivity tensor for the model in (10)*, according to* (11) *yields*

$$\widetilde{\boldsymbol{\varepsilon}}=-\varepsilon_r\varepsilon_0\boldsymbol{I}, \tag{12}$$

with $\boldsymbol{I}$ the second order identity tensor. Clearly, the expression in (12) *does not depend with respect to $\boldsymbol{F}$. A simple model embedding nonlinear dependence of $\widetilde{\boldsymbol{\varepsilon}}$ with respect to deformations (i.e with respect to $\boldsymbol{F}$) is widely used in the literature [32]*

$$\Psi_{em}(\boldsymbol{F},\boldsymbol{E}_0)=-\frac{\varepsilon_1}{2J}II_{\boldsymbol{HE}_0}-\frac{\varepsilon_2}{2}II_{\boldsymbol{FE}_0}-\frac{\varepsilon_3}{2}II_{\boldsymbol{E}_0}. \tag{13}$$

According to (11)*, the spatial permittivity tensor for the model in* (13) *is*

$$\widetilde{\boldsymbol{\varepsilon}}=-\varepsilon_1\boldsymbol{I}-\frac{\varepsilon_2}{J}\boldsymbol{b}^2-\frac{\varepsilon_3}{J}\boldsymbol{b}, \tag{14}$$

where $\boldsymbol{b}=\boldsymbol{F}\boldsymbol{F}^T$ represents the left Cauchy-Green strain tensor. An alternative way of incorporating nonlinearity into $\widetilde{\boldsymbol{\varepsilon}}$ can be achieved by considering a nonlinear susceptibility χ into the simple model in (10)*, namely*

$$\Psi_{em}(\boldsymbol{F},\boldsymbol{E}_0)=-\frac{\varepsilon_r(\boldsymbol{F})\varepsilon_0}{2J}II_{\boldsymbol{HE}_0};\qquad \varepsilon_r(\boldsymbol{F})=1+\chi(\boldsymbol{F}), \tag{15}$$

where $\chi(\boldsymbol{F})$ must be an isotropic and objective function of $\boldsymbol{F}$. For the model in (15)*, its associated spatial permittivity tensor $\widetilde{\boldsymbol{\varepsilon}}$ is*

$$\widetilde{\boldsymbol{\varepsilon}} = -(1+\chi(\boldsymbol{F}))\varepsilon_0 \boldsymbol{I}. \tag{16}$$

Notice however that the model in (13) *introduces a more complex nonlinear dependence with respect to $\boldsymbol{F}$ (see equation* (14)*) than the model in* (15)*, since the permittivity for the model in* (15) *is indeed isotropic irrespectively of the state of deformation (i.e. proportional to the identity tensor). For the numerical examples considered in Section 4, the simple constitutive model introduced in equation* (10) *will be considered without loss of generality. Incorporation of the more complex and realistic models in* (13) *and* (15) *into the topology optimisation framework developed in Section 3 would be immediate.*

Remark. *As already discussed in the previous remark, the constitutive model considered in this paper is, by no means, the most generic of all, as it does not embed all the possible physical phenomena inherent to dielectric elastomers. For instance, extensibility limit is not incorporated in the mechanical component $\Psi_m(\boldsymbol{F})$ in* (7)*. This can be achieved by means of alternative models such as the Gent model [7], defined as*

$$\Psi_m(\boldsymbol{F}) = -\frac{\mu J_{lim}}{2}\ln\Big(1-\frac{II_{\boldsymbol{F}}-3}{J_{lim}}\Big), \tag{17}$$

where μ refers to the shear modulus in the origin and J_{lim}, to the extensibility limit of the material. Another limitation of the model resides in its deterministic nature, i.e. aleatory uncertainty in the material properties of the model (electric permittivity, mechanical parameters, etc.) is not considered, despite the remarkable effect that these may have on the design of these materials (i.e. dielectric elastomers).

The aforementioned limitations can be incorporated into the topology optimisation framework developed subsequently in Section 3. However, despite the limitations of the simplified model considered, this does encapsulate inherent sources of electromechanically induced instabilities. Specifically, it is well-known that the electromechanical contribution $\Psi_{em}(\boldsymbol{F},\boldsymbol{E}_0)$ in (10) *permits the development of instabilities such as buckling, wrinkling and crumpling [71] beyond a critical value of electric field. These instabilities are prone to appear in the scenario considered on this paper, where an electric voltage gradient is applied across the extremely thin thickness of the material. However, the consideration of large values of electric field, which may trigger these instabilities, poses a tremendous challenge when making use of a gradient algorithm as that advocated for on this manuscript (see Section 3). Therefore, moderate values of the applied electric field will be considered in the numerical examples in Section 4, with the aim of preventing these scenarios.*

2.3. Variational formulation in reversible nonlinear electromechanics

The variational formulation associated with equations (2) and (3) is presented in this section. Specifically, the classical two-field variational principle with unknown fields $\boldsymbol{\phi} \in \mathbb{V}^{\boldsymbol{\phi}}$ and $\varphi \in \mathbb{V}^{\varphi}$ is advocated for in this paper, with $\mathbb{V}^{\boldsymbol{\phi}}, \mathbb{V}^{\varphi}$ functional spaces complying with the Dirichlet boundary conditions in (2d) and (3d), namely

$$\mathbb{V}^{\boldsymbol{\phi}} = \{\boldsymbol{\phi} \in (H^1(\mathcal{B}_0))^3 : \text{s.t.}\,(2\text{d})\}; \qquad \mathbb{V}^{\varphi} = \{\varphi \in H^1(\mathcal{B}_0) : \text{s.t.}\,(3\text{d})\}. \tag{18}$$

The variational principle is stated as follows

$$\Pi(\boldsymbol{\phi}^*,\varphi^*) = \inf_{\boldsymbol{\phi}}\sup_{\varphi}\left\{\int_{\mathcal{B}_0}\Psi\left(\boldsymbol{F},\boldsymbol{E}_0\right)\,dV - \Pi^m_{\text{ext}}\left(\boldsymbol{\phi}\right) - \Pi^{em}_{\text{ext}}\left(\varphi\right)\right\}, \tag{19}$$

where Π^m_{ext} and Π^{em}_{ext} represent the external work associated with the mechanical and electrical PDEs in (2) and (3), respectively, defined as

$$\Pi^m_{\text{ext}}\left(\boldsymbol{\phi}\right) = \int_{\mathcal{B}_0}\boldsymbol{f}_0\cdot\boldsymbol{\phi}\,dV + \int_{\partial_{\boldsymbol{t}}\mathcal{B}_0}\boldsymbol{t}_0\cdot\boldsymbol{\phi}\,dA; \qquad \Pi^{em}_{\text{ext}}\left(\varphi\right) = -\int_{\mathcal{B}_0}\rho_0\varphi\,dV - \int_{\partial_{\omega}\mathcal{B}_0}\omega_0\varphi\,dA. \tag{20}$$

The stationary conditions of $\Pi(\boldsymbol{\phi},\varphi)$ (19), yield the weak forms of the PDEs in (2) and (3), namely

$$D\Pi(\boldsymbol{\phi},\varphi)[\delta\boldsymbol{\phi}] = \int_{\mathcal{B}_0}\boldsymbol{P}\left(\boldsymbol{F},\boldsymbol{E}_0\right):\boldsymbol{\nabla}_0\delta\boldsymbol{\phi}\,dV - D\Pi^m_{\text{ext}}\left(\boldsymbol{\phi}\right)[\delta\boldsymbol{\phi}] = 0; \tag{21a}$$

$$D\Pi(\boldsymbol{\phi},\varphi)[\delta\varphi] = \int_{\mathcal{B}_0}\boldsymbol{D}_0\left(\boldsymbol{F},\boldsymbol{E}_0\right)\cdot\boldsymbol{\nabla}_0\delta\varphi\,dV - D\Pi^{em}_{\text{ext}}\left(\varphi\right)[\delta\varphi] = 0, \tag{21b}$$

where $\delta\boldsymbol{\phi} \in \mathbb{V}^{\boldsymbol{\phi}}_0$ and $\delta\varphi \in \mathbb{V}^{\varphi}_0$ represent independent virtual variations [2], with

$$D\Pi^m_{\text{ext}}\left(\boldsymbol{\phi}\right)[\delta\boldsymbol{\phi}] = \int_{\mathcal{B}_0}\boldsymbol{f}_0\cdot\delta\boldsymbol{\phi}\,dV + \int_{\partial_{\boldsymbol{t}}\mathcal{B}_0}\boldsymbol{t}_0\cdot\delta\boldsymbol{\phi}\,dA; \qquad D\Pi^{em}_{\text{ext}}\left(\varphi\right)[\delta\varphi] = -\int_{\mathcal{B}_0}\rho_0\delta\varphi\,dV - \int_{\partial_{\omega}\mathcal{B}_0}\omega_0\delta\varphi\,dA. \tag{22a}$$

[2] As usual, the sub-index 0 for a functional space is used to indicate satisfaction of homogeneous essential boundary conditions.

The solution of the coupled system of nonlinear weak forms in (21) is obtained through the use of a k-iterative scheme such as the Newton-Raphson. This entails the linearisation of both weak forms in (21) with respect to increments in the solution fields $\Delta\boldsymbol{\phi} \in \mathbb{V}_0^{\boldsymbol{\phi}}$ and $\Delta\varphi \in \mathbb{V}_0^{\varphi}$ as

$$D^2\Pi(\boldsymbol{\phi}^k, \varphi^k)[\delta\boldsymbol{\phi}; \Delta\boldsymbol{\phi}] + D^2\Pi(\boldsymbol{\phi}^k, \varphi^k)[\delta\boldsymbol{\phi}; \Delta\varphi] = -D\Pi(\boldsymbol{\phi}^k, \varphi^k)[\delta\boldsymbol{\phi}]; \tag{23a}$$

$$D^2\Pi(\boldsymbol{\phi}^k, \varphi^k)[\delta\varphi; \Delta\boldsymbol{\phi}] + D^2\Pi(\boldsymbol{\phi}^k, \varphi^k)[\delta\varphi; \Delta\varphi] = -D\Pi(\boldsymbol{\phi}^k, \varphi^k)[\delta\varphi], \tag{23b}$$

From (23), the solution field $\{\boldsymbol{\phi}, \varphi\}$ at iteration k are updated according to

$$\boldsymbol{\phi}^{k+1} = \boldsymbol{\phi}^k + \Delta\boldsymbol{\phi}; \qquad \varphi^{k+1} = \varphi^k + \Delta\varphi. \tag{24}$$

In equations (23), the terms on the left-hand side can be obtained as

$$\begin{aligned}
D^2\Pi(\boldsymbol{\phi}, \varphi)[\delta\boldsymbol{\phi}; \Delta\boldsymbol{\phi}] &= \int_{\mathcal{B}_0} \boldsymbol{\nabla}_0\delta\boldsymbol{\phi} : \boldsymbol{\mathcal{C}}\left(\boldsymbol{F}, \boldsymbol{E}_0\right) : \boldsymbol{\nabla}_0\Delta\boldsymbol{\phi}\, dV; \qquad & D^2\Pi(\boldsymbol{\phi}, \varphi)[\delta\boldsymbol{\phi}; \Delta\varphi] &= \int_{\mathcal{B}_0} \boldsymbol{\nabla}_0\delta\boldsymbol{\phi} : \boldsymbol{\mathcal{P}}^T\left(\boldsymbol{F}, \boldsymbol{E}_0\right) \cdot \boldsymbol{\nabla}_0\Delta\varphi\, dV; \\
D^2\Pi(\boldsymbol{\phi}, \varphi)[\delta\varphi; \Delta\boldsymbol{\phi}] &= \int_{\mathcal{B}_0} \boldsymbol{\nabla}_0\delta\varphi \cdot \boldsymbol{\mathcal{P}}\left(\boldsymbol{F}, \boldsymbol{E}_0\right) : \boldsymbol{\nabla}_0\Delta\boldsymbol{\phi}\, dV; \qquad & D^2\Pi(\boldsymbol{\phi}, \varphi)[\delta\varphi; \Delta\varphi] &= -\int_{\mathcal{B}_0} \boldsymbol{\nabla}_0\delta\varphi \cdot \boldsymbol{\varepsilon}\left(\boldsymbol{F}, \boldsymbol{E}_0\right) \boldsymbol{\nabla}_0\Delta\varphi\, dV,
\end{aligned} \tag{25}$$

with $\boldsymbol{\mathcal{C}}$, $\boldsymbol{\mathcal{P}}$ and $\boldsymbol{\varepsilon}$ defined in (5) and where $\left(\boldsymbol{\mathcal{P}}^T\right)_{jJI} = (\boldsymbol{\mathcal{P}})_{IjJ}$.

3. Topology optimisation framework

3.1. Phase-field formulation

In this section, the underlying fabrication principle for the design of shape-morphing DE-based devices through a multi-material-based approach is presented. Figure 3 depicts a multilayered device with intercalated electrodes of alternating polarity, spreading over the entire faces of the elastomers. The objective is to create an non-uniform distribution of electric field both across the thickness and over the in-plane direction of the three layers. For that, N different DE materials ($N = 3$ in Figure 4), with differentiated mechanical and electrical properties can be combined appropriately on each layer with the aim of attaining potentially complex shape morphing configurations.

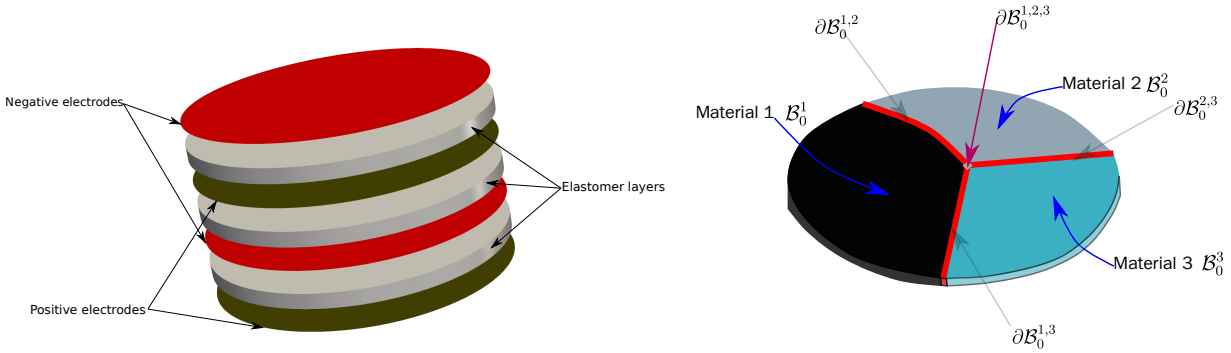

(a) (b)

Figure 3: (a) Device comprising three layers with intercalated electrodes; (b) One of the various elastomeric layers across the thickness of the device and the various regions $\{\mathcal{B}_0^1, \mathcal{B}_0^2, \mathcal{B}_0^3, \partial\mathcal{B}_0^{1,2}, \partial\mathcal{B}_0^{1,3}, \partial\mathcal{B}_0^{2,3}, \partial\mathcal{B}_0^{1,2,3}\}$ for the particular case of three different DE materials.

For the case considered in Figure 4, three different materials are considered potentially spreading over each of the three layers of the device. For convenience, these will be denoted as *Material 1*, *Material 2* and *Material 3*. Each of them is characterised by suitable free energy density functions $\Psi(\boldsymbol{F}, \boldsymbol{E}_0)$ (6). Thus, *Material 1* is characterised by the free energy density function $\Psi = \Psi_1(\boldsymbol{F}, \boldsymbol{E}_0)$. Similarly, *Material 2* and *Material 3* are characterised by the free energy density functions $\Psi = \Psi_2(\boldsymbol{F}, \boldsymbol{E}_0)$ and $\Psi = \Psi_3(\boldsymbol{F}, \boldsymbol{E}_0)$, respectively. A smooth representation of the topology of each of the $N = 3$ materials (i.e. *Material 1*, *Material 2* and *Material 3*) present over each of the various layers of the device is adopted. For that, $N - 1 = 2$ phase-field functions $\psi_i \in \mathbb{V}^{\psi_i}$ (with $i = \{1, 2\}$) are introduced on each layer, being

$$\mathbb{V}^{\psi_i} = \left\{\psi_i : \mathcal{B}_0 \to [0, 1]\,, \quad \psi_i \in H^1(\mathcal{B}_0), \quad i = \{1, \ldots, N\}\right\}. \tag{26}$$

Crucially, the extreme values (i.e. 0 or 1) of the two phase-field functions $\psi_1(\mathcal{B}_0)$ and $\psi_2(\mathcal{B}_0)$, would determine the regions $\mathcal{B}_0^1$, $\mathcal{B}_0^2$ and $\mathcal{B}_0^3$ corresponding with the presence of *Material 1*, *Material 2* and *Material 3*, respectively,

with $\mathcal{B}_0^1 \cup \mathcal{B}_0^2 \cup \mathcal{B}_0^1 \subset \mathcal{B}_0$. This can be mathematically stated as below

$$\forall \boldsymbol{X} \in \mathcal{B}_0^i, \begin{cases} \psi_1(\boldsymbol{X}) = 1; & \text{if } \Psi(\boldsymbol{F}, \boldsymbol{E}_0) = \Psi_1(\boldsymbol{F}, \boldsymbol{E}_0) \quad (\mathcal{B}_0^1 \text{ or } \textit{Material 1}); \\ \psi_1(\boldsymbol{X}) = 0,\ \psi_2(\boldsymbol{X}) = 1; & \text{if } \Psi(\boldsymbol{F}, \boldsymbol{E}_0) = \Psi_2(\boldsymbol{F}, \boldsymbol{E}_0) \quad (\mathcal{B}_0^2 \text{ or } \textit{Material 2}); \\ \psi_1(\boldsymbol{X}) = 0,\ \psi_2(\boldsymbol{X}) = 0; & \text{if } \Psi(\boldsymbol{F}, \boldsymbol{E}_0) = \Psi_3(\boldsymbol{F}, \boldsymbol{E}_0) \quad (\mathcal{B}_0^3 \text{ or } \textit{Material 3}). \end{cases} \tag{27}$$

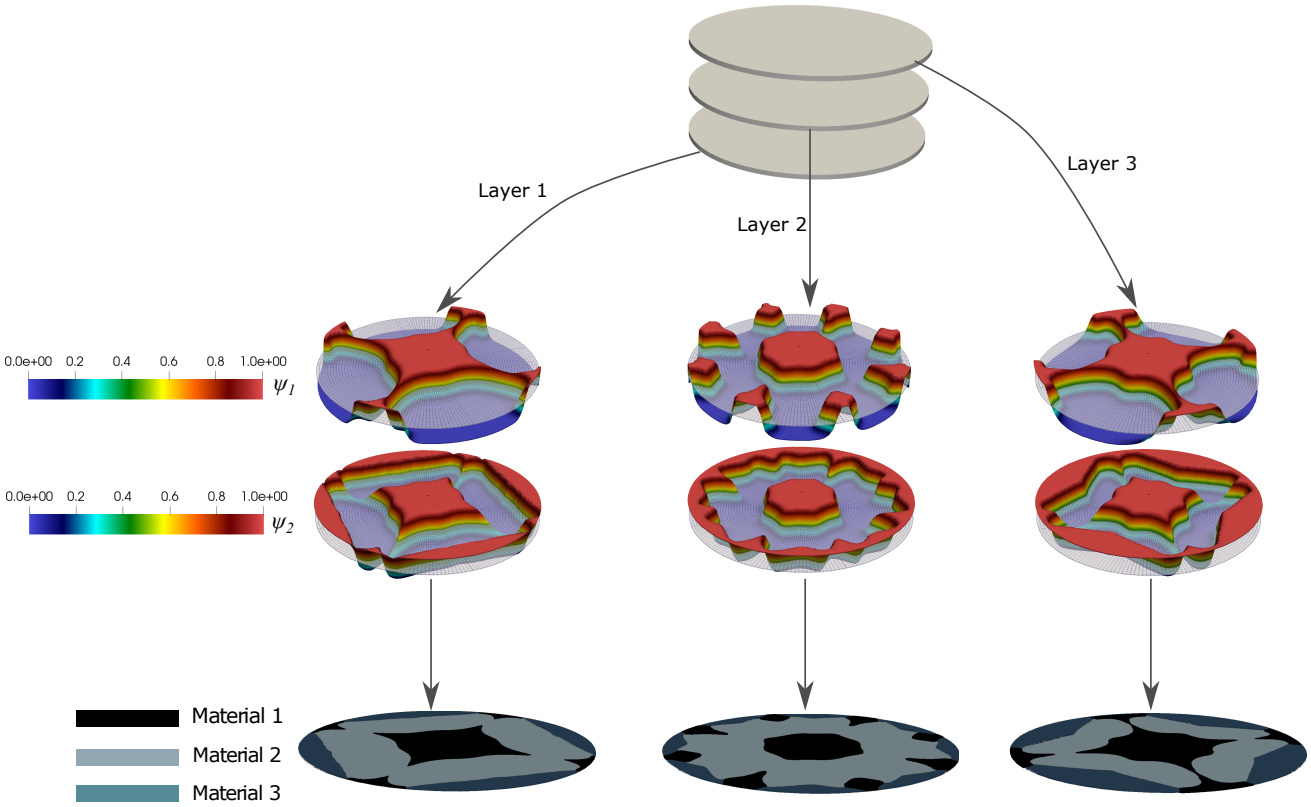

Figure 4: *top*: actuator with three layers across its thickness (the layers have been presented separately for visualisation purposes); *middle*: the two phase-field functions $\psi_1(\boldsymbol{X})$ and $\psi_2(\boldsymbol{X})$ over each layer; *bottom*: "reconstruction" of the regions associated with the three different materials through evaluation of the phase-field functions $\psi_1(\boldsymbol{X})$ and $\psi_2(\boldsymbol{X})$ according to (27).

Intermediate values of $\psi_1(\mathcal{B}_0)$ and $\psi_2(\mathcal{B}_0)$ would correspond with the smooth representation of the shared boundaries between the three subsets $\{\mathcal{B}_0^1, \mathcal{B}_0^2, \mathcal{B}_0^3\}$. Three of the possible "smooth" boundaries are detoned as $\partial\mathcal{B}_0^{1,2}$, $\partial\mathcal{B}_0^{1,3}$ and $\partial\mathcal{B}_0^{2,3}$, and correspond with the boundary shared by the pairs of regions $\mathcal{B}_0^1$ and $\mathcal{B}_0^2$, $\mathcal{B}_0^1$ and $\mathcal{B}_0^3$, and finally, by $\mathcal{B}_0^2$ and $\mathcal{B}_0^3$, respectively. A fourth "smooth" boundary, denoted as $\partial\mathcal{B}_0^{1,2,3}$, would correspond with the region shared by the three subsets $\mathcal{B}_0^1$, $\mathcal{B}_0^2$ and $\mathcal{B}_0^3$ (see Figure 3_b). This entails that in our smooth approach, $\mathcal{B}_0$ can be represented as the union of the following subsets

$$\mathcal{B}_0 = \underbrace{\mathcal{B}_0^1 \cup \mathcal{B}_0^2 \cup \mathcal{B}_0^3}_{\text{regions with a single material}} \cup \underbrace{\partial\mathcal{B}_0^{1,2} \cup \partial\mathcal{B}_0^{1,3} \cup \partial\mathcal{B}_0^{2,3}}_{\text{regions with mixture of two materials}} \cup \underbrace{\partial\mathcal{B}_0^{1,2,3}}_{\text{region with mixture of three materials}} \tag{28}$$

Notice from equation (27), that for the limiting values of the phase-field functions $\{\psi_1(\boldsymbol{X}), \psi_2(\boldsymbol{X})\}$, it is clear that the free energy function $\Psi(\boldsymbol{F}, \boldsymbol{E}_0)$ must coincide with that of the material associated with either of the three regions $\mathcal{B}_0^i$ ($i = \{1, 2, 3\}$). However, the definition of $\Psi(\boldsymbol{F}, \boldsymbol{E}_0)$ is not that obvious over the "smooth" boundaries $\{\partial\mathcal{B}_0^{1,2}, \partial\mathcal{B}_0^{1,3}, \partial\mathcal{B}_0^{2,3}, \partial\mathcal{B}_0^{1,2,3}\}$, namely

$$\forall \boldsymbol{X} \in \mathcal{B}_0^i, \begin{cases} 0 < \psi_1(\boldsymbol{X}) < 1,\ \psi_2(\boldsymbol{X}) = 1; & \text{unknown expression for } \Psi(\boldsymbol{F}, \boldsymbol{E}_0) \quad (\text{region } \partial\mathcal{B}_0^{1,2}); \\ 0 < \psi_1(\boldsymbol{X}) < 1,\ \psi_2(\boldsymbol{X}) = 0; & \text{unknown expression for } \Psi(\boldsymbol{F}, \boldsymbol{E}_0) \quad (\text{region } \partial\mathcal{B}_0^{1,3}); \\ \psi_1(\boldsymbol{X}) = 0,\ 0 < \psi_2(\boldsymbol{X}) < 1; & \text{unknown expression for } \Psi(\boldsymbol{F}, \boldsymbol{E}_0) \quad (\text{region } \partial\mathcal{B}_0^{2,3}); \\ 0 < \psi_1(\boldsymbol{X}) < 1,\ 0 < \psi_2(\boldsymbol{X}) < 1; & \text{unknown expression for } \Psi(\boldsymbol{F}, \boldsymbol{E}_0) \quad (\text{region } \partial\mathcal{B}_0^{1,2,3}); \end{cases} \tag{29}$$

The definition of $\Psi(\boldsymbol{F}, \boldsymbol{E}_0)$ over $\{\partial\mathcal{B}_0^{1,2}, \partial\mathcal{B}_0^{1,3}, \partial\mathcal{B}_0^{2,3}, \partial\mathcal{B}_0^{1,2,3}\}$ is dictated by choice of the so-called *energy interpolation scheme*, which at least must comply with the limiting cases shown in equation (27). For that, we

incorporate both phase-field functions $\{\psi_1(\boldsymbol{X}), \psi_2(\boldsymbol{X})\}$ as arguments of the free energy, i.e.

$$\Psi = \bar{\Psi}(\psi_1(\boldsymbol{X}), \psi_2(\boldsymbol{X}), \boldsymbol{F}, \boldsymbol{E}_0). \tag{30}$$

Specifically, we propose the following energy interpolation scheme when there are three materials available

$$\bar{\Psi}(\psi_1(\boldsymbol{X}), \psi_2(\boldsymbol{X}), \boldsymbol{F}, \boldsymbol{E}_0) = \Big(\psi_1(\boldsymbol{X})\Big)^p \Psi_1(\boldsymbol{F}, \boldsymbol{E}_0) + \Big(1 - (\psi_1(\boldsymbol{X}))^p\Big)\Big((\psi_2(\boldsymbol{X}))^p \Psi_2(\boldsymbol{F}, \boldsymbol{E}_0) + (1 - (\psi_2(\boldsymbol{X}))^p) \Psi_3(\boldsymbol{F}, \boldsymbol{E}_0)\Big). \tag{31}$$

Typically, a value of $p = 3$ is used for the penalising exponent in (31) in the context of density-based TO, which in turn, ensures the satisfaction of Hashin-Shtrikman bounds [72] in the specific case of linearised elasticity. Essentially, the phase-field function $\psi_1(\boldsymbol{X})$ is introduced in order to differentiate in a smooth manner between two material phases. These correspond with *Material 1* and a composite material resulting from the mixture of both *Material 2* and *Material 3*. The second phase-field function, namely $\psi_2(\boldsymbol{X})$, is introduced within this composite in order to differentiate in a smooth manner between the material phases associated with *Material 2* and *Material 3*. This is illustrated in Figure 5.

Associated with the interpolated free energy density $\bar{\Psi}(\psi_1(\boldsymbol{X}), \psi_2(\boldsymbol{X}), \boldsymbol{F}, \boldsymbol{E}_0)$ in (31), it is now possible to obtain the first Piola-Kirchhoff stress tensor $\boldsymbol{P}$ and electric displacement field $\boldsymbol{D}_0$ according to (4), yielding

$$\boldsymbol{P}(\psi_1(\boldsymbol{X}), \psi_2(\boldsymbol{X}), \boldsymbol{F}, \boldsymbol{E}_0) = \Big(\psi_1(\boldsymbol{X})\Big)^p \boldsymbol{P}_1 + \Big(1 - (\psi_1(\boldsymbol{X}))^p\Big)\Big((\psi_2(\boldsymbol{X}))^p \boldsymbol{P}_2 + (1 - (\psi_2(\boldsymbol{X}))^p) \boldsymbol{P}_3\Big); \tag{32a}$$

$$\boldsymbol{D}_0(\psi_1(\boldsymbol{X}), \psi_2(\boldsymbol{X}), \boldsymbol{F}, \boldsymbol{E}_0) = \Big(\psi_1(\boldsymbol{X})\Big)^p \boldsymbol{D}_{0_1} + \Big(1 - (\psi_1(\boldsymbol{X}))^p\Big)\Big((\psi_2(\boldsymbol{X}))^p \boldsymbol{D}_{0_2} + (1 - (\psi_2(\boldsymbol{X}))^p) \boldsymbol{D}_{0_3}\Big), \tag{32b}$$

where the individual contributions $\{\boldsymbol{P}_1, \boldsymbol{P}_2, \boldsymbol{P}_3\}$ and $\{\boldsymbol{D}_{0_1}, \boldsymbol{D}_{0_2}, \boldsymbol{D}_{0_3}\}$ are defined according to (4), namely

$$\boldsymbol{P}_i = \partial_{\boldsymbol{F}} \bar{\Psi}_i(\boldsymbol{F}, \boldsymbol{E}_0); \qquad \boldsymbol{D}_{0_i} = -\partial_{\boldsymbol{E}_0} \bar{\Psi}_i(\boldsymbol{F}, \boldsymbol{E}_0); \qquad (i = \{1, 2, 3\}). \tag{33}$$

Similarly, the constitutive tensors $\{\boldsymbol{\mathcal{C}}, \boldsymbol{\mathcal{P}}, \boldsymbol{\varepsilon}\}$ associated with $\bar{\Psi}(\psi_1(\boldsymbol{X}), \psi_2(\boldsymbol{X}), \boldsymbol{F}, \boldsymbol{E}_0)$ (refer to equation (31)) can be obtained simply from (5), resulting in

$$\boldsymbol{\mathcal{C}}(\psi_1(\boldsymbol{X}), \psi_2(\boldsymbol{X}), \boldsymbol{F}, \boldsymbol{E}_0) = \Big(\psi_1(\boldsymbol{X})\Big)^p \boldsymbol{\mathcal{C}}_1 + \Big(1 - (\psi_1(\boldsymbol{X}))^p\Big)\Big((\psi_2(\boldsymbol{X}))^p \boldsymbol{\mathcal{C}}_2 + (1 - (\psi_2(\boldsymbol{X}))^p) \boldsymbol{\mathcal{C}}_3\Big); \tag{34a}$$

$$\boldsymbol{\mathcal{P}}(\psi_1(\boldsymbol{X}), \psi_2(\boldsymbol{X}), \boldsymbol{F}, \boldsymbol{E}_0) = \Big(\psi_1(\boldsymbol{X})\Big)^p \boldsymbol{\mathcal{P}}_1 + \Big(1 - (\psi_1(\boldsymbol{X}))^p\Big)\Big((\psi_2(\boldsymbol{X}))^p \boldsymbol{\mathcal{P}}_2 + (1 - (\psi_2(\boldsymbol{X}))^p) \boldsymbol{\mathcal{P}}_3\Big); \tag{34b}$$

$$\boldsymbol{\varepsilon}(\psi_1(\boldsymbol{X}), \psi_2(\boldsymbol{X}), \boldsymbol{F}, \boldsymbol{E}_0) = \Big(\psi_1(\boldsymbol{X})\Big)^p \boldsymbol{\varepsilon}_1 + \Big(1 - (\psi_1(\boldsymbol{X}))^p\Big)\Big((\psi_2(\boldsymbol{X}))^p \boldsymbol{\varepsilon}_2 + (1 - (\psi_2(\boldsymbol{X}))^p) \boldsymbol{\varepsilon}_3\Big), \tag{34c}$$

where the individual contributions $\{\boldsymbol{\mathcal{C}}_1, \boldsymbol{\mathcal{C}}_2, \boldsymbol{\mathcal{C}}_3\}$, $\{\boldsymbol{\mathcal{P}}_1, \boldsymbol{\mathcal{P}}_2, \boldsymbol{\mathcal{P}}_3\}$ and $\{\boldsymbol{\varepsilon}_1, \boldsymbol{\varepsilon}_2, \boldsymbol{\varepsilon}_3\}$ are defined according to (5), namely

$$\boldsymbol{\mathcal{C}}_i = \partial^2_{\boldsymbol{F}\boldsymbol{F}} \bar{\Psi}_i(\boldsymbol{F}, \boldsymbol{E}_0); \qquad \boldsymbol{\mathcal{P}}_i = -\partial^2_{\boldsymbol{E}_0\boldsymbol{F}} \bar{\Psi}_i(\boldsymbol{F}, \boldsymbol{E}_0); \qquad \boldsymbol{\varepsilon}_i = -\partial^2_{\boldsymbol{E}_0\boldsymbol{E}_0} \bar{\Psi}_i(\boldsymbol{F}, \boldsymbol{E}_0); \qquad i = \{1, 2, 3\}. \tag{35}$$

Remark. *The energy interpolation scheme in equation* (31) *has been particularised for the case when three different DE materials are considered. For the more generic case when N materials are considered, it would be possible to generalise the energy interpolation scheme through the introduction of $N-1$ phase field functions $\{\psi_1(\boldsymbol{X}), \psi_2(\boldsymbol{X}), \ldots, \psi_{N-1}(\boldsymbol{X})\}$ according to the following and convenient nested definition of the final interpolated energy $\bar{\Psi}(\psi_1(\boldsymbol{X}), \ldots, \psi_{N-1}(\boldsymbol{X}), \boldsymbol{F}, \boldsymbol{E}_0)$ as*

$$\begin{aligned}
\bar{\Psi}(\psi_1(\boldsymbol{X}), \ldots, \psi_{N-1}(\boldsymbol{X}), \boldsymbol{F}, \boldsymbol{E}_0) &= \Big(\psi_1(\boldsymbol{X})\Big)^p \Psi_1(\boldsymbol{F}, \boldsymbol{E}_0) + \Big(1 - (\psi_1(\boldsymbol{X}))^p\Big) \bar{\Psi}_{2,\ldots,N}(\psi_2(\boldsymbol{X}), \ldots, \psi_{N-1}(\boldsymbol{X}), \boldsymbol{F}, \boldsymbol{E}_0);\\
\bar{\Psi}_{2,\ldots,N}(\psi_2(\boldsymbol{X}), \ldots, \psi_{N-1}(\boldsymbol{X}), \boldsymbol{F}, \boldsymbol{E}_0) &= \Big(\psi_2(\boldsymbol{X})\Big)^p \Psi_2(\boldsymbol{F}, \boldsymbol{E}_0) + \Big(1 - (\psi_2(\boldsymbol{X}))^p\Big) \bar{\Psi}_{3,\ldots,N}(\psi_3(\boldsymbol{X}), \ldots, \psi_{N-1}(\boldsymbol{X}), \boldsymbol{F}, \boldsymbol{E}_0);\\
&\vdots \quad \vdots\\
&\vdots \quad \vdots\\
&\vdots \quad \vdots\\
\bar{\Psi}_{N-2,\ldots,N}(\psi_{N-2}(\boldsymbol{X}), \psi_{N-1}(\boldsymbol{X}), \boldsymbol{F}, \boldsymbol{E}_0) &= \Big(\psi_{N-2}(\boldsymbol{X})\Big)^p \Psi_{N-2}(\boldsymbol{F}, \boldsymbol{E}_0) + \Big(1 - (\psi_{N-2}(\boldsymbol{X}))^p\Big) \bar{\Psi}_{N-1,N}(\psi_{N-1}(\boldsymbol{X}), \boldsymbol{F}, \boldsymbol{E}_0);\\
\bar{\Psi}_{N-1,N}(\psi_{N-1}(\boldsymbol{X}), \boldsymbol{F}, \boldsymbol{E}_0) &= \Big(\psi_{N-1}(\boldsymbol{X})\Big)^p \Psi_{N-1}(\boldsymbol{F}, \boldsymbol{E}_0) + \Big(1 - (\psi_{N-1}(\boldsymbol{X}))^p\Big) \Psi_N(\boldsymbol{F}, \boldsymbol{E}_0).
\end{aligned} \tag{36}$$

Notice that in (36)*, we have introduced the notation $\bar{\Psi}_{i,i+1,\ldots,N}$ to refer to the free energy density whose homogenised behaviour depends upon the phase-field functions $\{\psi_i(\boldsymbol{X}), \ldots, \psi_{N-1}(\boldsymbol{X})\}$. Hence, the proposed homogenised behaviour of $\bar{\Psi}_{i,i+1,\ldots,N}$ corresponds to the mixture of Material i, Material $i+1$, up to Material N.*

Remark. *Some authors [37, 73], rather than the free energy density $\Psi(\boldsymbol{F}, \boldsymbol{E}_0)$, prefer to define the constitutive model of dielectric elastomers using its dual energetic counterpart, denoted as internal energy $e(\boldsymbol{F}, \boldsymbol{D}_0)$. Both are related through the following standard Legendre transformation*

$$\Psi(\boldsymbol{F}, \boldsymbol{E}_0) = -\sup_{\boldsymbol{D}_0}\{\boldsymbol{E}_0 \cdot \boldsymbol{D}_0 - e(\boldsymbol{F}, \boldsymbol{D}_0)\}. \tag{37}$$

A similar energy interpolation scheme to that considered in equation (31) *can also be used for the internal energy-based approach. This will be explained for the case where the interpolation scheme in* (31) *is particularised to two materials. Given that the energy interpolation scheme represents in fact a mathematical artifact (it is not physical) permitting interpolation between two different models, there is not just a unique definition for such interpolation. Indeed, one possible energy interpolation scheme would be analogous to that in* (31)*, namely*

$$\bar{e}(\psi_1(\boldsymbol{X}), \boldsymbol{F}, \boldsymbol{D}_0) = \Big(\psi_1(\boldsymbol{X})\Big)^p e_1(\boldsymbol{F}, \boldsymbol{D}_0) + \Big(1 - (\psi_1(\boldsymbol{X}))^p\Big) e_2(\boldsymbol{F}, \boldsymbol{D}_0). \tag{38}$$

where e_1 and e_2 refer to the internal energies of the two materials corresponding with a value of the phase-field $\psi = 1$ and $\psi = 0$, respectively. Alternatively, a second energy interpolation scheme can be defined, distinguishing between the mechanical and electromechanical contributions of the internal energy, as follows

$$\begin{aligned}\bar{e}(\psi_1(\boldsymbol{X}), \boldsymbol{F}, \boldsymbol{D}_0) = &\Big(\psi_1(\boldsymbol{X})\Big)^p e_{m1}(\boldsymbol{F}) + \Big(1 - (\psi_1(\boldsymbol{X}))^p\Big) e_{m2}(\boldsymbol{F}) \\ &+ \frac{e_{em1}(\boldsymbol{F}, \boldsymbol{D}_0) e_{em2}(\boldsymbol{F}, \boldsymbol{D}_0)}{\psi_1(\boldsymbol{X}^p)\left(e_{em2}(\boldsymbol{F}, \boldsymbol{D}_0) - e_{em1}(\boldsymbol{F}, \boldsymbol{D}_0)\right) + e_{em1}(\boldsymbol{F}, \boldsymbol{D}_0)},\end{aligned} \tag{39}$$

where e_{mi} and e_{emi} represent the purely mechanical and electromechanical contributions of the internal energy density of material i. Notice that the last term on the right-hand side of (39) *(and its partial derivatives) coincides with $e_{em1}(\boldsymbol{F}, \boldsymbol{D}_0)$ for $\psi(\boldsymbol{X}) = 1$ and with $e_{em2}(\boldsymbol{F}, \boldsymbol{D}_0)$ for $\psi(\boldsymbol{X}) = 0$. The interpolation scheme in* (39) *introduces, however, a higher degree of nonlinearity compared to that in equation* (38)*.*

3.2. Mathematical formulation

The final objective of combining N number of materials per layer is to create a non-uniform electric field with the aim of permitting the DE-based device to attain a complex target configuration. Essentially, this is a design problem with an *objective function*, denoted as $\mathcal{J}(\boldsymbol{\phi})$ that needs to be minimised. The latter, for the specific type of shape-morphing application considered on this paper, can be defined as

$$\mathcal{J}(\boldsymbol{\phi}) = \frac{1}{2}\int_D ||\boldsymbol{\phi}(\boldsymbol{X}) - \boldsymbol{\phi}^*(\boldsymbol{X})||^2 \, dV, \tag{40}$$

with $D \subseteq \mathcal{B}_0$, and where $\boldsymbol{\phi}^*$ represents the target configuration that the final DE-based device needs to attain. The associated design optimisation problem can then be formulated as follows

$$(P)\begin{cases} \min\limits_{\psi_1(\boldsymbol{X}), \psi_2(\boldsymbol{X})} \mathcal{J}(\boldsymbol{\phi}) \text{ (40)}; \\ \text{s.t} \begin{cases} \text{Variational statements (21)}; \\ \text{Constitutive model (31)}; \\ 0 \leq \psi_1(\boldsymbol{X}) \leq 1; \quad \psi_1(\boldsymbol{X}) \in H^1(\mathcal{B}_0); \\ 0 \leq \psi_2(\boldsymbol{X}) \leq 1; \quad \psi_2(\boldsymbol{X}) \in H^1(\mathcal{B}_0); \end{cases} \end{cases} \tag{41}$$

In this paper, a gradient method is pursued for the optimal solution of the optimisation problem (P) in (41). With that aim, it is customary to introduce a Lagrangian functional whose sensitivity is crucial in order to let the gradient algorithm to converge towards the final optimal solution in an iterative fashion. The definition of this Lagrangian and the non-standard derivation of its sensitivity is carried out in the forthcoming sections.

3.3. The optimisation Lagrangian $\mathcal{L}$ and its sensitivity

For problem (P), presented in equation (41), the Lagrangian functional $\mathcal{L}$ can be defined as

$$\mathcal{L}(\psi_1, \psi_2, \boldsymbol{\phi}, \varphi, \boldsymbol{p}_{\boldsymbol{\phi}}, p_\varphi) = \mathcal{J}(\boldsymbol{\phi}) - D\Pi(\psi_1, \psi_2, \boldsymbol{\phi}, \varphi)[\boldsymbol{p}_{\boldsymbol{\phi}}] - D\Pi(\psi_1, \psi_2, \boldsymbol{\phi}, \varphi)[p_\varphi], \tag{42}$$

where $D\Pi(\psi_1, \psi_2, \boldsymbol{\phi}, \varphi)[\boldsymbol{p}_{\boldsymbol{\phi}}]$ and $D\Pi(\psi_1, \psi_2, \boldsymbol{\phi}, \varphi)[p_\varphi]$ represent the weak forms in equation (2) and (3), respectively. Furthemore, $\boldsymbol{p}_{\boldsymbol{\phi}} \in \mathbb{V}_0^{\boldsymbol{\phi}}$ and $p_\varphi \in \mathbb{V}_0^{\varphi}$ represent the corresponding adjoint state variables. Notice that these terms are identical to those featuring in (21a) and (21b), just replacing $\delta\boldsymbol{\phi}$ with $\boldsymbol{p}_{\boldsymbol{\phi}}$) and $\delta\varphi$ with p_φ. Associated with

the Lagrangian $\mathcal{L}$ in (42), we compute its optimality conditions. The optimality conditions of $\mathcal{L}$ with respect to the adjoint states $\{\boldsymbol{p}_{\boldsymbol{\phi}}, p_\varphi\}$ are defined as

$$D\mathcal{L}(\psi_1,\psi_2,\boldsymbol{\phi},\varphi,\boldsymbol{p}_{\boldsymbol{\phi}},p_\varphi)[\delta\boldsymbol{p}_{\boldsymbol{\phi}}] = -D\Pi(\psi_1,\psi_2,\boldsymbol{\phi},\varphi)[\delta\boldsymbol{p}_{\boldsymbol{\phi}}] = 0; \tag{43a}$$

$$D\mathcal{L}(\psi_1,\psi_2,\boldsymbol{\phi},\varphi,\boldsymbol{p}_{\boldsymbol{\phi}},p_\varphi)[\delta p_\varphi] = -D\Pi(\psi_1,\psi_2,\boldsymbol{\phi},\varphi)[\delta p_{\boldsymbol{\varphi}}] = 0, \tag{43b}$$

where $\delta\boldsymbol{p}_\phi \in \mathbb{V}_0^{\boldsymbol{\phi}}$ and $\delta p_\varphi \in \mathbb{V}_0^{\varphi}$ represent virtual variations of the corresponding adjoint states. Solution of (43) permits to obtain the unknown fields $\{\boldsymbol{\phi},\varphi\}$. Notice that the first Piola-Kirchhoff stress tensor $\boldsymbol{P}$ and the Lagrangian electric displacement field $\boldsymbol{D}_0$ featuring in (43) (see (21)) are computed according to equation (32), which complies with the energy interpolation scheme in (31).

Furthermore, the optimality conditions of $\mathcal{L}$ with respect to the fields $\{\boldsymbol{p}_{\boldsymbol{\phi}}, p_\varphi\}$ yield

$$\begin{aligned} D\mathcal{L}(\psi_1,\psi_2,\boldsymbol{\phi},\varphi,\boldsymbol{p}_{\boldsymbol{\phi}},p_\varphi)[\delta\boldsymbol{\phi}] = &- D^2\Pi(\psi_1,\psi_2,\boldsymbol{\phi},\varphi,\boldsymbol{p}_{\boldsymbol{\phi}},p_\varphi)[\boldsymbol{p}_{\boldsymbol{\phi}};\delta\boldsymbol{\phi}] - D^2\Pi(\psi_1,\psi_2,\boldsymbol{\phi},\varphi)[p_\varphi;\delta\boldsymbol{\phi}] \\ &+ D\mathcal{J}(\boldsymbol{\phi})[\delta\boldsymbol{\phi}] = 0; \end{aligned} \tag{44a}$$

$$D\mathcal{L}(\psi_1,\psi_2,\boldsymbol{\phi},\varphi,\boldsymbol{p}_{\boldsymbol{\phi}},p_\varphi)[\delta\varphi] = - D^2\Pi(\psi_1,\psi_2,\boldsymbol{\phi},\varphi)[\boldsymbol{p}_{\boldsymbol{\phi}};\delta\varphi] - D^2\Pi(\psi_{\mathcal{B}_0}(\psi_1,\psi_2,\boldsymbol{\phi},\varphi)[p_\varphi;\delta\varphi] = 0, \tag{44b}$$

where the second directional derivatives of Π featuring in (44) are presented in (25), just by replacing $\{\delta\boldsymbol{\phi},\delta\varphi\}$ with $\{\boldsymbol{p}_{\boldsymbol{\phi}},p_\varphi\}$, and $\{\Delta\boldsymbol{\phi},\Delta\varphi\}$ with $\{\delta\boldsymbol{\phi},\delta\varphi\}$, respectively. In addition, the constitutive tensors $\{\boldsymbol{\mathcal{C}},\boldsymbol{\mathcal{P}},\boldsymbol{\varepsilon}\}$ featuring in the second directional derivatives in (44) (see (25)) are computed according to equation (34), which complies with the energy interpolation scheme in (31). Solution of the above linear equations in (44) enables to obtain the adjoint states $\{\boldsymbol{p}_{\boldsymbol{\phi}},p_\varphi\}$.

Crucially, solution of the fields $\{\boldsymbol{\phi},\varphi\}$ and the adjoint states $\{\boldsymbol{p}_{\boldsymbol{\phi}},p_\varphi\}$ from (43) and (44), respectively, permits to address the ultimate goal of this section, namely, to obtain the sensitivity of the Lagrangian $\mathcal{L}$ with respect $\{\psi_1,\psi_2\}$, namely $D\mathcal{L}[\Delta\psi_1]$ and $D\mathcal{L}[\Delta\psi_2]$ which yield

$$\begin{aligned} D\mathcal{L}[\Delta\psi_1] &= -D^2\Pi(\psi_1,\psi_2,\boldsymbol{\phi},\varphi,\boldsymbol{p}_{\boldsymbol{\phi}},p_\varphi)[\boldsymbol{p}_{\boldsymbol{\phi}};\Delta\psi_1] - D^2\Pi(\psi_1,\psi_2,\boldsymbol{\phi},\varphi,\boldsymbol{p}_{\boldsymbol{\phi}},p_\varphi)[p_\varphi;\Delta\psi_1]; \\ D\mathcal{L}[\Delta\psi_2] &= -D^2\Pi(\psi_1,\psi_2,\boldsymbol{\phi},\varphi,\boldsymbol{p}_{\boldsymbol{\phi}},p_\varphi)[\boldsymbol{p}_{\boldsymbol{\phi}};\Delta\psi_2] - D^2\Pi(\psi_1,\psi_2,\boldsymbol{\phi},\varphi,\boldsymbol{p}_{\boldsymbol{\phi}},p_\varphi)[p_\varphi;\Delta\psi_2]. \end{aligned} \tag{45}$$

Making use of the definition of both $D\Pi[\boldsymbol{p}_{\boldsymbol{\phi}}]$ and $D\Pi[\boldsymbol{p}_\varphi]$ in (21) (by replacing $\{\delta\boldsymbol{\phi},\delta\varphi\}$ with $\{\boldsymbol{p}_{\boldsymbol{\phi}},p_\varphi\}$), both sensitivities in (45) can be defined as

$$\begin{aligned} D\mathcal{L}[\Delta\psi_1] &= -\int_{\mathcal{B}_0} \Delta\psi_1 \Big(\underbrace{\partial_{\psi_1}\boldsymbol{P}\left(\psi_1(\boldsymbol{X}),\psi_2(\boldsymbol{X}),\boldsymbol{F},\boldsymbol{E}_0\right) : \boldsymbol{\nabla}_0\boldsymbol{p}_{\boldsymbol{\phi}} + \partial_{\psi_1}\boldsymbol{D}_0\left(\psi_1(\boldsymbol{X}),\psi_2(\boldsymbol{X}),\boldsymbol{F},\boldsymbol{E}_0\right)\cdot\boldsymbol{\nabla}_0 p_\varphi}_{\mathcal{G}_{\psi_1}(\boldsymbol{X})} \Big)\, dV; \\ D\mathcal{L}[\Delta\psi_2] &= -\int_{\mathcal{B}_0} \Delta\psi_2 \Big(\underbrace{\partial_{\psi_2}\boldsymbol{P}\left(\psi_1(\boldsymbol{X}),\psi_2(\boldsymbol{X}),\boldsymbol{F},\boldsymbol{E}_0\right) : \boldsymbol{\nabla}_0\boldsymbol{p}_{\boldsymbol{\phi}} + \partial_{\psi_2}\boldsymbol{D}_0\left(\psi_1(\boldsymbol{X}),\psi_2(\boldsymbol{X}),\boldsymbol{F},\boldsymbol{E}_0\right)\cdot\boldsymbol{\nabla}_0 p_\varphi}_{\mathcal{G}_{\psi_2}(\boldsymbol{X})} \Big)\, dV, \end{aligned} \tag{46}$$

where the partial derivatives $\{\partial_{\psi_1}\boldsymbol{P},\partial_{\psi_2}\boldsymbol{P}\}$ and $\{\partial_{\psi_1}\boldsymbol{D}_0,\partial_{\psi_2}\boldsymbol{D}_0\}$ in (46) can be simply obtained from the definition in equation (32), complying with the energy interpolation scheme in equation (31), yielding

$$\partial_{\psi_1}\boldsymbol{P}(\psi_1(\boldsymbol{X}),\psi_2(\boldsymbol{X}),\boldsymbol{F},\boldsymbol{E}_0) = p\Big(\psi_1(\boldsymbol{X})\Big)^{p-1}\left(\boldsymbol{P}_1 - \Big(\left(\psi_2(\boldsymbol{X})\right)^p\boldsymbol{P}_2 + \left(1-\left(\psi_2(\boldsymbol{X})\right)^p\right)\boldsymbol{P}_3\Big)\right); \tag{47a}$$

$$\partial_{\psi_2}\boldsymbol{P}(\psi_1(\boldsymbol{X}),\psi_2(\boldsymbol{X}),\boldsymbol{F},\boldsymbol{E}_0) = p\Big(1-\left(\psi_1(\boldsymbol{X})\right)^p\Big)\Big(\psi_2(\boldsymbol{X})\Big)^{p-1}\Big(\boldsymbol{P}_2-\boldsymbol{P}_3\Big); \tag{47b}$$

$$\partial_{\psi_1}\boldsymbol{D}_0(\psi_1(\boldsymbol{X}),\psi_2(\boldsymbol{X}),\boldsymbol{F},\boldsymbol{E}_0) = p\Big(\psi_1(\boldsymbol{X})\Big)^{p-1}\left(\boldsymbol{D}_{0_1} - \Big(\left(\psi_2(\boldsymbol{X})\right)^p\boldsymbol{D}_{0_2} + \left(1-\left(\psi_2(\boldsymbol{X})\right)^p\right)\boldsymbol{D}_{0_3}\Big)\right); \tag{47c}$$

$$\partial_{\psi_2}\boldsymbol{D}_0(\psi_1(\boldsymbol{X}),\psi_2(\boldsymbol{X}),\boldsymbol{F},\boldsymbol{E}_0) = p\Big(1-\left(\psi_1(\boldsymbol{X})\right)^p\Big)\Big(\psi_2(\boldsymbol{X})\Big)^{p-1}\Big(\boldsymbol{D}_{0_2}-\boldsymbol{D}_{0_3}\Big). \tag{47d}$$

As already stated, the sensitivities $\{D\mathcal{L}[\Delta\psi_1],D\mathcal{L}[\Delta\psi_2]\}$, dictate the evolution of both phase-field functions $\{\psi_1,\psi_2\}$. This is shown in the following section.

3.4. Evolution of the phase-field functions

In order to describe the evolution of regions $\mathcal{B}_0^1$, $\mathcal{B}_0^2$ and $\mathcal{B}_0^3$ (when three different DE materials are considered), a pseudo-time parameter $\tau \in [\tau_0,\tau_m]$ is introduced. In this work, the evolution of the phase-field functions $\psi_1(\boldsymbol{X})$ and $\psi_2(\boldsymbol{X})$, used to describe regions $\mathcal{B}_0^1$, $\mathcal{B}_0^2$ and $\mathcal{B}_0^3$, is carried out using the Allen-Cahn approach (see [42]). The

following initial boundary value problem can be used for the evolution of each of the phase-field functions $\{\psi_1, \psi_2\}$ as

$$\begin{cases} \partial_\tau \psi_i = \kappa \boldsymbol{\nabla}_0^2 \psi_i - \partial_{\psi_i} \left(\dfrac{1}{4} \Phi(\psi_i) + \eta\, \mathcal{G}_{\psi_i}(\boldsymbol{X}) h(\psi_i) \right); & \text{in } \mathcal{B}_0 \times [\tau_0, \tau_m]; \\ 0 = \boldsymbol{\nabla}_0 \psi_i \cdot \boldsymbol{N}|_{\partial \mathcal{B}_0}; & \text{on } \partial\mathcal{B}_0 \times [\tau_0, \tau_m]; \\ \psi_i|_{\tau_0} = \psi_i^0; & \text{in } \mathcal{B}_0; \end{cases} \qquad i = \{1, 2\}. \tag{48}$$

In equation (48), $\kappa \geq 0$ and $\eta \geq 0$, $\mathcal{G}_{\psi_1}(\boldsymbol{X})$ and $\mathcal{G}_{\psi_2}(\boldsymbol{X})$ are indeed the sensitivity per unit volume of the Lagrangian $\mathcal{L}$ in (42) with respect to the phase-field functions $\{\psi_1(\boldsymbol{X}), \psi_2(\boldsymbol{X})\}$, presented in equation (46). In addition, in (48) $\Phi(\psi_i)$ and $h(\psi_i)$ (for $i = \{1, 2\}$) are polynomials given by

$$\Phi(\psi_i) = \psi_i^2 (1 - \psi_i)^2; \qquad h(\psi_i) = \psi_i^3 (6\psi_i^2 - 15\psi_i + 10); \qquad i = \{1, 2\}, \tag{49}$$

where $\Phi(\psi_i)$ denotes the double well potential. Furthermore, $h(\psi_i)$ in (49) represents a polynomial complying with $h'(\psi_i) = 30\Phi(\psi_i)$ and $h(0) = 0$. The first term on the right-hand side of (48) represents a diffusion term acting only acts on the phase transition region whilst the second term on the right-hand side of (48) involves the sensitivities $\{\mathcal{G}_{\psi_1}, \mathcal{G}_{\psi_2}\}$ in (46), in addition to the double well potential (refer to Figure 5). The variational form for the evolution equation in (48) can be defined as

$$\begin{aligned} \int_{\mathcal{B}_0} \partial_\tau \psi_i \delta\psi_i \, dV &= -\int_{\mathcal{B}_0} \kappa \boldsymbol{\nabla}_0 \psi_i \cdot \boldsymbol{\nabla}_0 \delta\psi_i \, dV + \int_{\mathcal{B}_0} \psi_i (1 - \psi_i) r(\boldsymbol{X}, \psi_i) \delta\psi_i \, dV; \\ \psi_i|_{\tau_0} &= \psi_i^0; \quad \text{in } \mathcal{B}_0, \end{aligned} \qquad i = \{1, 2\} \tag{50}$$

where $\delta\psi_i \in \mathbb{V}_0^{\psi_i}$ (with $\mathbb{V}_0^{\psi_i}$ in (26)), $i = \{1, 2\}$ are suitable virtual fields and the scalar field $r(\boldsymbol{X}, \psi_i)$ ($i = \{1, 2\}$) are given by

$$r(\boldsymbol{X}, \psi_i) = \psi_i - \frac{1}{2} - 30\eta \mathcal{G}_{\psi_i}(\boldsymbol{X}) \psi_i (1 - \psi_i); \qquad i = \{1, 2\}. \tag{51}$$

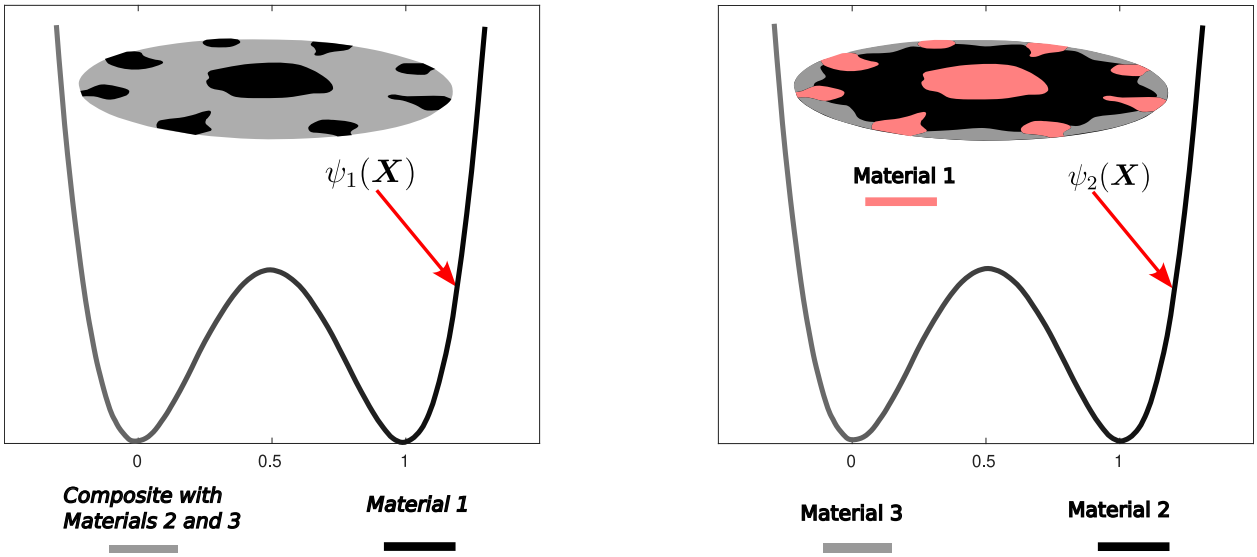

Figure 5: Double well potential representation. *Left:* double well for phase-field function $\psi_1(\boldsymbol{X})$, modelling the transition between *Material 1* and the composite material with phases corresponding to *Materials 2* and *3*. *Right:* double well for phase-field function $\psi_2(\boldsymbol{X})$, modelling the transition between *Material 2* and *Material 3*.

Remark. *In order to permit an independent evolution of both phase-field functions $\{\psi_1(\boldsymbol{X}), \psi_2(\boldsymbol{X})\}$ at each of the various layers across the thickness of the device, we only enforce $\mathcal{C}^0$ continuity for both functions within each layer. This entails that both functions $\{\psi_1(\boldsymbol{X}), \psi_2(\boldsymbol{X})\}$ are discontinuous in the thickness direction exactly at the interface between elastomeric layers, but continuous within every layer.*

3.5. Pseudo-time marching scheme

Following [42] and considering the pseudo-time interval $[\tau_n, \tau_{n+1}]$ with $\Delta\tau = \tau_{n+1} - \tau_n$, a semi-implicit one-step marching scheme can be used to advance the solution from ψ_i^n to ψ_i^{n+1} via time discretisation of (50) as

$$\mathcal{T}(\psi_i^{n+1}) = \int_{\mathcal{B}_0} \left[\left(\frac{\psi_i^{n+1} - \psi_i^n}{\Delta\tau} \right) \delta\psi_i + \kappa \boldsymbol{\nabla}_0 \psi_i^{n+1} \cdot \boldsymbol{\nabla}_0 \delta\psi_i - S(\psi_i^n, \psi_i^{n+1}) r(\boldsymbol{X}, \psi_i^n) \delta\psi_i \right] dV = 0; \qquad i = \{1, 2\}, \tag{52}$$

with

$$S(\psi_i^n, \psi_i^{n+1}) = \begin{cases} \psi_i^{n+1}(1-\psi_i^n); & \text{if } r(\boldsymbol{X}, \psi_i^n) \leq 0; \\ \psi_i^n(1-\psi_i^{n+1}); & \text{if } r(\boldsymbol{X}, \psi_i^n) > 0. \end{cases} \tag{53}$$

Solution of the linear equation (52) is obtained as

$$D\mathcal{T}(\psi_i)[\Delta\psi_i] = -\mathcal{T}(\psi_i^n); \qquad \psi_i^{n+1} = \psi_i^n + \Delta\psi_i; \qquad i = \{1, 2\}. \tag{54}$$

3.6. Algorithmic flowchart

Algorithm 1 summarises the flowchart of actions of the phase-field-based multi-material design platform.

Algorithm 1 Pseudo-code of phase-field multi-material topology optimisation approach

Initialisation of phase-field functions $\{\psi_1(\boldsymbol{X}), \psi_2(\boldsymbol{X}), \ldots, \psi_{N-1}(\boldsymbol{X})\}$

Initialise pseudo-time: $\tau = 0$

Solve $\{\boldsymbol{\phi}, \varphi\}$ from optimality condition (43)

Solve $\{\boldsymbol{p}_{\boldsymbol{\phi}}, p_\varphi\}$ from optimality condition (44)

Evaluate objective function $\mathcal{J}(\boldsymbol{\phi})|_{\tau=0}$

Set optimisation parameters $\{\Delta\tau, \kappa, \eta\}$ for (52)-(53)

Define optimisation tolerance ($tol.$) and variable $e > tol.$

while $e > tol.$ **do**
  $\tau \leftarrow \tau + \Delta\tau$

  Get sensitivities $\mathcal{G}_{\psi_i}$ $(i = \{1, 2, \ldots, N-1\})$ from (46)

  Evolve phase-field functions ψ_i $(i = \{1, 2, \ldots, N-1\})$ using (52)-(53)

  if $\psi_i > 1$ **then**
    $\psi_i = 1$
  else
    Do not correct
  end if

  if $\psi_i < 0$ **then**
    $\psi_i = 0$
  else
    Do not correct
  end if

  Solve $\{\boldsymbol{\phi}, \varphi\}$ from optimality condition (43)

  Solve $\{\boldsymbol{p}_{\boldsymbol{\phi}}, p_\varphi\}$ from optimality condition (44)

  Evaluate objective function $\mathcal{J}(\boldsymbol{\phi})|_\tau$

  Define $e = \mathcal{J}|_\tau - \mathcal{J}|_{\tau-\Delta\tau}$
end while

4. Numerical examples

This section presents a series of numerical examples with the aim of evaluating the proposed multi-material topology optimisation formulation. In all the examples included, tri-quadratic Finite Element interpolations for both displacement and electric potential fields have been considered. The underlying reason for this specific choice of interpolation lies on the nearly-incompressible nature of DEs and the consideration of DE devices with extremely small thickness (in comparison with the in-plane dimensions of the device). These two features pose limitations for the consideration of low order finite element discretisations, as these tend to exhibit various sources of locking, i.e. volumetric and bending locking [73, 74].

In all the examples, three different DE materials will be considered. These will be denoted as *Material 1*, *Material 2* and *Material 3*, in order to be consistent with the notation used in Section 3. The constitutive model of the three materials comprises a Mooney-Rivlin model (see equation (7)) for the mechanical contribution of the

free energy density, namely $\Psi_m(\boldsymbol{F})$, and an ideal dielectric elastomer (see equation (10)) for the electromechanical energy contribution $\Psi_{em}(\boldsymbol{F}, \boldsymbol{E}_0)$. The difference between the three materials resides in the material parameters used. The values for these can be found in Table 1.

	μ_1 (Pa)	μ_2 (Pa)	λ (Pa)	ε_r	$\{f_m, f_e\}$
Material 1	5×10^4	5×10^4	10^8	4.8	-
Material 2	15×10^4	15×10^4	3×10^8	24	$f_m = 3, f_e = 5$
Material 3	1.5×10^4	1.5×10^4	3×10^7	0.048	$f_m = 0.3, f_e = 0.01$

Table 1: Material parameters for the constitutive model used for *Material 1*, *Material 2* and *Material 3*. See equations (7) and (10). Parameters $\{f_m, f_e\}$ represent the mechanical and electrical contrasts, which scale the material parameters of the models for *Material 2* and *Material 3* with respect to those of *Material 1*.

As it can be seen from Table 1, *Material 2* is stiffer than *Material 1*. However, its relative permittivity ε_r is larger, which may enable *Material 2* to undergo larger electrically induced deformations than *Material 1* for the same value of applied electric field. On the other hand, *Material 3*, although being the most flexible of the three materials, has a very low electric permittivity, being practically inactive from the electromechanical standpoint. The most optimal combination of these materials with the aim of attaining a given target configuration is therefore, far from intuitive. The objective of the following numerical examples is, therefore, to test the ability of the topology optimisation framework developed to propose optimal solutions for the topology of the regions where *Material 1*, *Material 2* and *Material 3*, need to be placed in the most convenient manner with a shape morphing objective in mind.

4.1. Numerical example 1

In this example, the geometry depicted in Figure 6_a is considered. The initial seed for the two phase-field functions $\{\psi_1(\boldsymbol{X})|_{\tau=0}, \psi_2(\boldsymbol{X})|_{\tau=0}\}$ (τ representing the pseudo-time parameter at $\tau = 0$) at the three layers across the thickness is shown in Figure $(6)_b$ (all layers are initialised identically), where the red colour corresponds with $\psi_i(\boldsymbol{X})|_{\tau=0} = 1$, $i = \{1, 2\}$ whilst the blue color corresponds with $\psi_i(\boldsymbol{X})|_{\tau=0} = 0$, $i = \{1, 2\}$. The Finite Element discretisation of the geometry is shown in Figure 6_a, with a total of 98415 nodes for both unknown fields $\{\boldsymbol{\phi}, \varphi\}$.

Two different shape morphing configurations have been studied in this example, Specifically, these corresponds with two different actuation modes, denoted as **actuation mode 1** and **actuation mode 2**. **Actuation mode 1** is achieved by minimising the vertical (Z direction) displacement of control points $\{B, D\}$ (see Figure 6_a), whilst maximising that of points $\{A, C\}$. **Actuation mode 2** is achieved through maximisation and minimisation of the vertical (Z direction) displacement of points $\{B, A, D, C\}$ and $\{E, H, G, C\}$, respectively. The mathematical expressions for their associated objective functions are the following

$$\mathcal{J}(\boldsymbol{\phi})|_{\text{mode1}} = \underbrace{-\left(\boldsymbol{\phi}(\boldsymbol{X}_A) - \boldsymbol{X}_A + \boldsymbol{\phi}(\boldsymbol{X}_C) - \boldsymbol{X}_C\right) \cdot \boldsymbol{E}_3}_{\text{Maximisation}} + \underbrace{\left(\boldsymbol{\phi}(\boldsymbol{X}_B) - \boldsymbol{X}_B + \boldsymbol{\phi}(\boldsymbol{X}_D) - \boldsymbol{X}_D\right) \cdot \boldsymbol{E}_3}_{\text{Minimisation}}; \tag{55a}$$

$$\begin{aligned}\mathcal{J}(\boldsymbol{\phi})|_{\text{mode2}} = &\underbrace{-\left(\boldsymbol{\phi}(\boldsymbol{X}_B) - \boldsymbol{X}_B + \boldsymbol{\phi}(\boldsymbol{X}_A) - \boldsymbol{X}_A + \boldsymbol{\phi}(\boldsymbol{X}_D) - \boldsymbol{X}_D + \boldsymbol{\phi}(\boldsymbol{X}_C) - \boldsymbol{X}_C\right) \cdot \boldsymbol{E}_3}_{\text{Maximisation}} \\ &\underbrace{+\left(\boldsymbol{\phi}(\boldsymbol{X}_E) - \boldsymbol{X}_E + \boldsymbol{\phi}(\boldsymbol{X}_H) - \boldsymbol{X}_H + \boldsymbol{\phi}(\boldsymbol{X}_G) - \boldsymbol{X}_G + \boldsymbol{\phi}(\boldsymbol{X}_F) - \boldsymbol{X}_F\right) \cdot \boldsymbol{E}_3}_{\text{Minimisation}}.\end{aligned} \tag{55b}$$

Figure 7_a shows the result of the topology optimisation algorithm for the objective function corresponding with **actuation mode 1**. Specifically, the regions where *Material 1, Material 2* and *Material 3* need to be placed at each of the three layers across the thickness are shown. Notice that these regions can be inferred from the values of the phase-field functions $\{\psi_1(\boldsymbol{X}), \psi_2(\boldsymbol{X})\}$ according to equation (27). In addition, the electrically induced deformation attained after the application of a voltage difference of value $\Delta\varphi = 2 \times 10^3$ (V) is also displayed in Figure 7_a. Clearly, the final shape of the electrically deformed DE design is in agreement with the objective function $\mathcal{J}(\boldsymbol{\phi})|_{\text{mode1}}$ in equation (55a).

On the other hand, Figure 7_b shows the result of the topology optimisation algorithm for the objective function corresponding with **actuation mode 2**, displaying the regions where *Material 1, Material 2* and *Material 3* need to be placed at each of the three layers across the thickness. In addition, the electrically induced deformation attained after the application of a voltage difference of value $\Delta\varphi = 2 \times 10^3$ (V) is also displayed in Figure 7_b. Clearly,

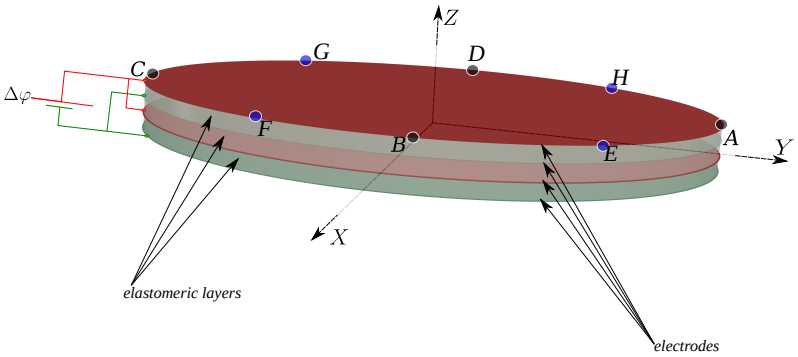

(a)

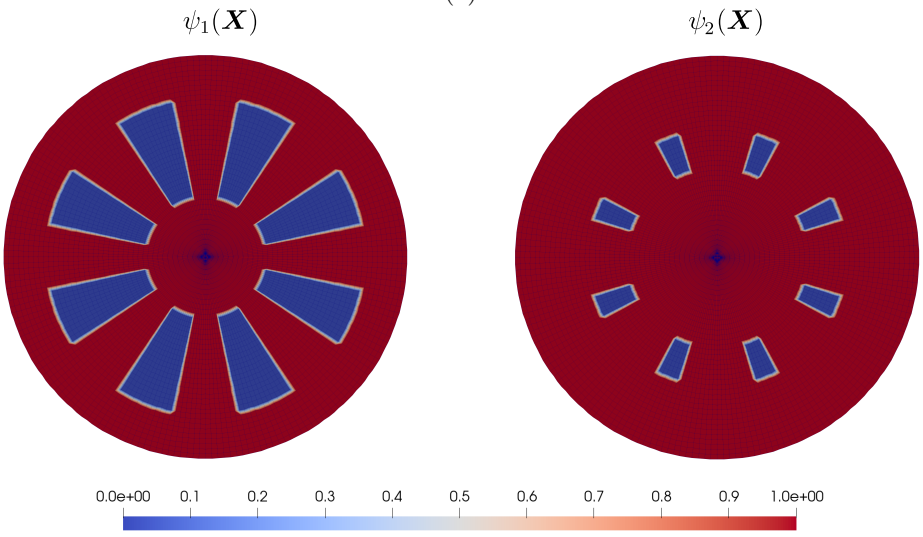

(b)

Figure 6: Example 1. (a) Geometry of the DE with radius $R = 0.035$ (m) and thickness of each of the three layers of $R/128$. Also shown the control points for inducing the desired actuation modes when electrical actuation is applied; (b) Common initial seed for the two phase-field functions $\{\psi_1(\boldsymbol{X}), \psi_2(\boldsymbol{X})\}$ for the three layers.

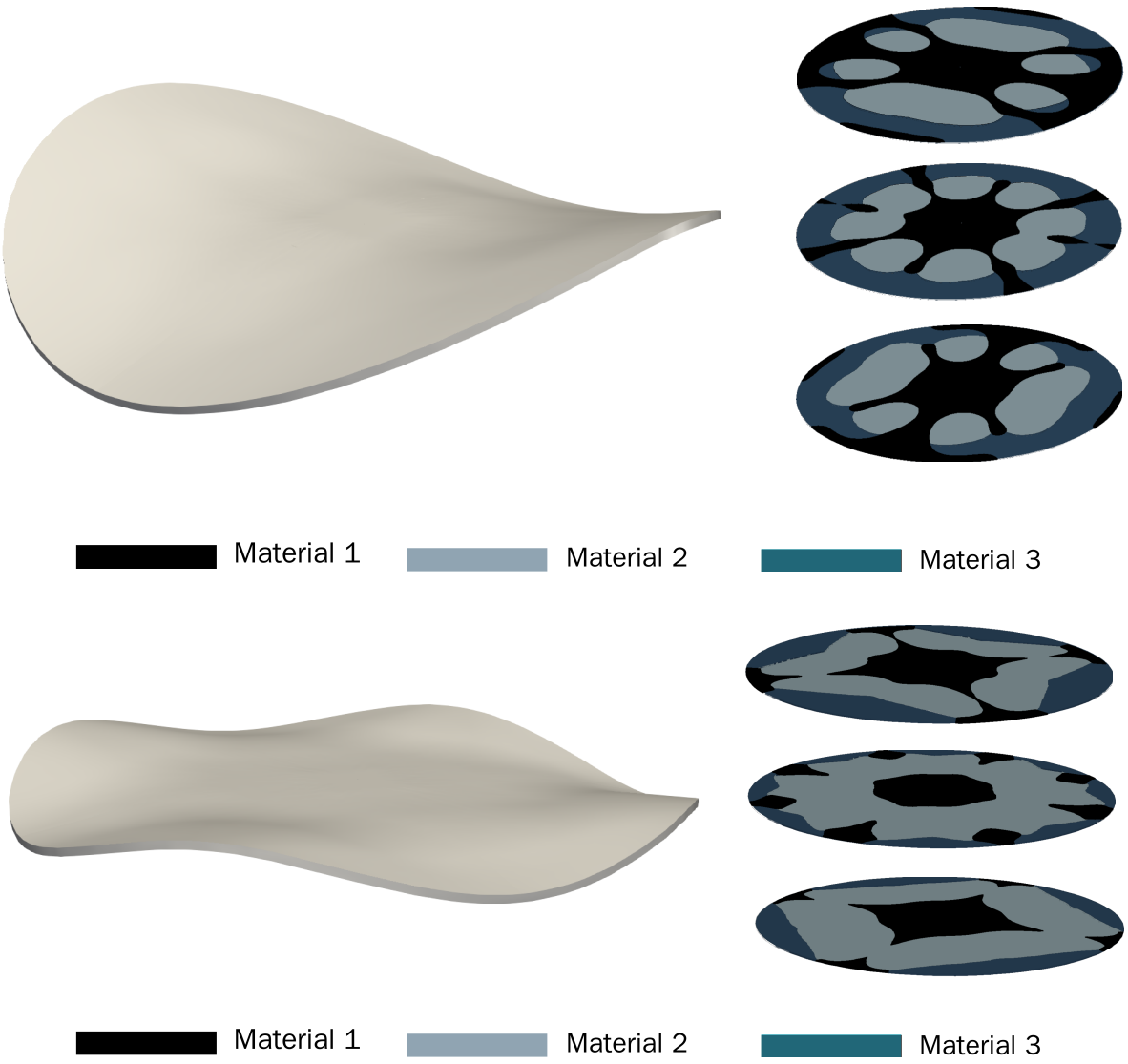

Figure 7: Example 1. *Top:* electrically induced deformation for optimal result corresponding with **actuation mode 1**, characterised by distribution of *Material 1*, *Material 2* and *Material 3* shown at each of the three layers. *Bottom:* electrically induced deformation for optimal result corresponding with **actuation mode 2**, characterised by distribution of *Material 1*, *Material 2* and *Material 3* shown at each of the three layers.

the final shape of the electrically deformed DE design is in agreement with the objective function $\mathcal{J}(\boldsymbol{\phi})|_{\text{mode2}}$ in equation (55b).

Notice that the objective functions considered for this example in equation (55) tend to maximise or minimise the displacement of specific control points. In that sense, this example does not strictly correspond with a true shape morphing application, where the distance to a predefined target shape is typically sought, in agreement with the expression in equation (40). This will be the object of the following two numerical examples.

4.2. Numerical example 2

In this example, the geometry depicted in Figure 8_a is considered. The initial seed for $\{\psi_1(\boldsymbol{X})|_{\tau=0}\,,\,\psi_2(\boldsymbol{X})|_{\tau=0}\}$ at the three layers across the thickness is shown in Figure 8_b (all layers are initialised in the same manner), where the red colour is associated with a value of $\psi_i(\boldsymbol{X})|_{\tau=0} = 1$, $i = \{1,2\}$ whilst the blue color is associated with $\psi_i(\boldsymbol{X})|_{\tau=0} = 0$, $i = \{1,2\}$. The different initialisation corresponds to the two different geometries considered, associated with the two actuation modes explored in this example. These will be denoted again as **actuation mode 1** and **actuation mode 2**. They are described in the next paragraph. The Finite Element discretisation, with a total of 113967 nodes for both unknown fields $\{\boldsymbol{\phi}, \varphi\}$, is also shown in Figure 8_b.

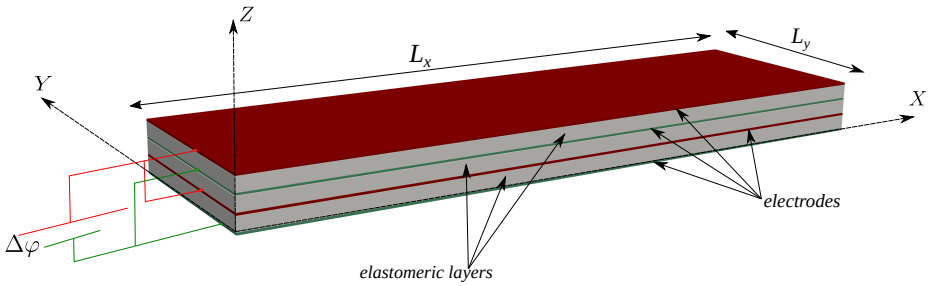

(a)

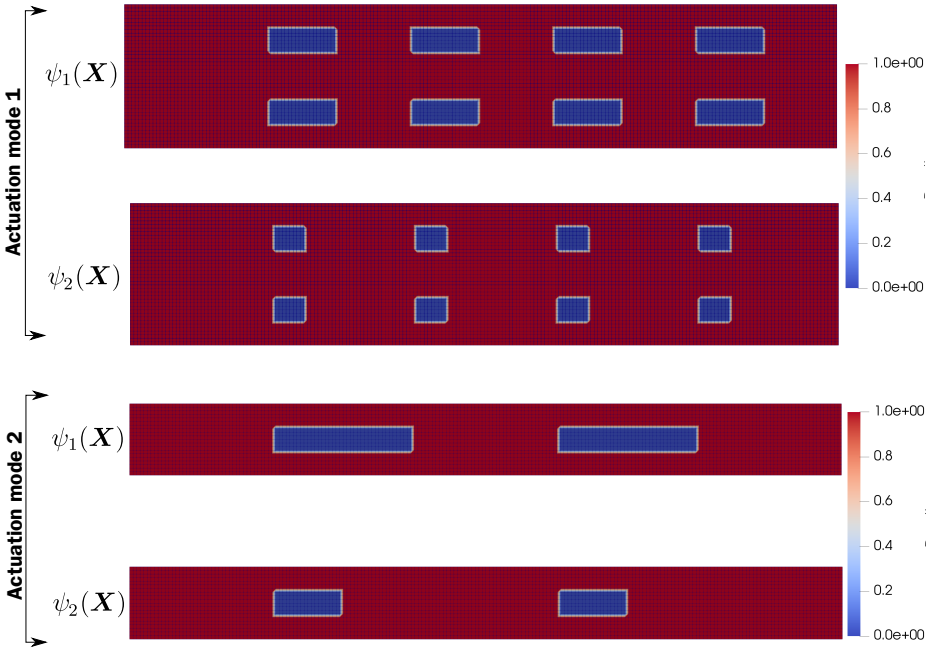

(b)

Figure 8: (a) Geometry of the DE. $\{L_X, L_Y\} = \{0.05, 0.01\}$ and thickness $h = L_X/360$ for **actuation mode 1**. $\{L_X, L_Y\} = \{0.05, 0.005\}$ and thickness $h = L_X/360$ for **actuation mode 2**. (b) Common initial seed for the two phase-field functions $\{\psi_1(\boldsymbol{X}), \psi_2(\boldsymbol{X})\}$ for the three layers for the two actuation modes considered in this example.

Two different designs have been investigated for the DE layout described above. These correspond with two different actuation modes described as follows. **Actuation mode 1** is induced by generating an electrically induced deformation similar to *letter L*, whereas **actuation mode 2** is induced by generating an electrically induced deformation similar to *letter S*. This has been mathematically enforced by defining the target configuration

$\boldsymbol{\phi}^\star$ for both actuation modes as

$$(\boldsymbol{\phi}^\star - \boldsymbol{X}) \cdot \boldsymbol{E}_1|_{\text{mode1}} = \begin{cases} 0, & X < \dfrac{L_X}{2} \\ -\left(X - \dfrac{L_X}{2}\right), & X >= \dfrac{L_X}{2} \end{cases} \tag{56a}$$

$$(\boldsymbol{\phi}^\star - \boldsymbol{X}) \cdot \boldsymbol{E}_3|_{\text{mode1}} = \begin{cases} 0, & X < \dfrac{L_X}{2} \\ \left(X - \dfrac{L_X}{2}\right), & X >= \dfrac{L_X}{2} \end{cases} \tag{56b}$$

$$(\boldsymbol{\phi}^\star - \boldsymbol{X}) \cdot \boldsymbol{E}_3|_{\text{mode2}} = \frac{L_X}{2}\left(\frac{\tanh(\beta\eta) + \tanh(\beta(X/L_X - \eta))}{\tanh(\beta\eta) + \tanh(\beta(1-\eta))}\right); \qquad \beta = 4,\ \eta = 0.5. \tag{56c}$$

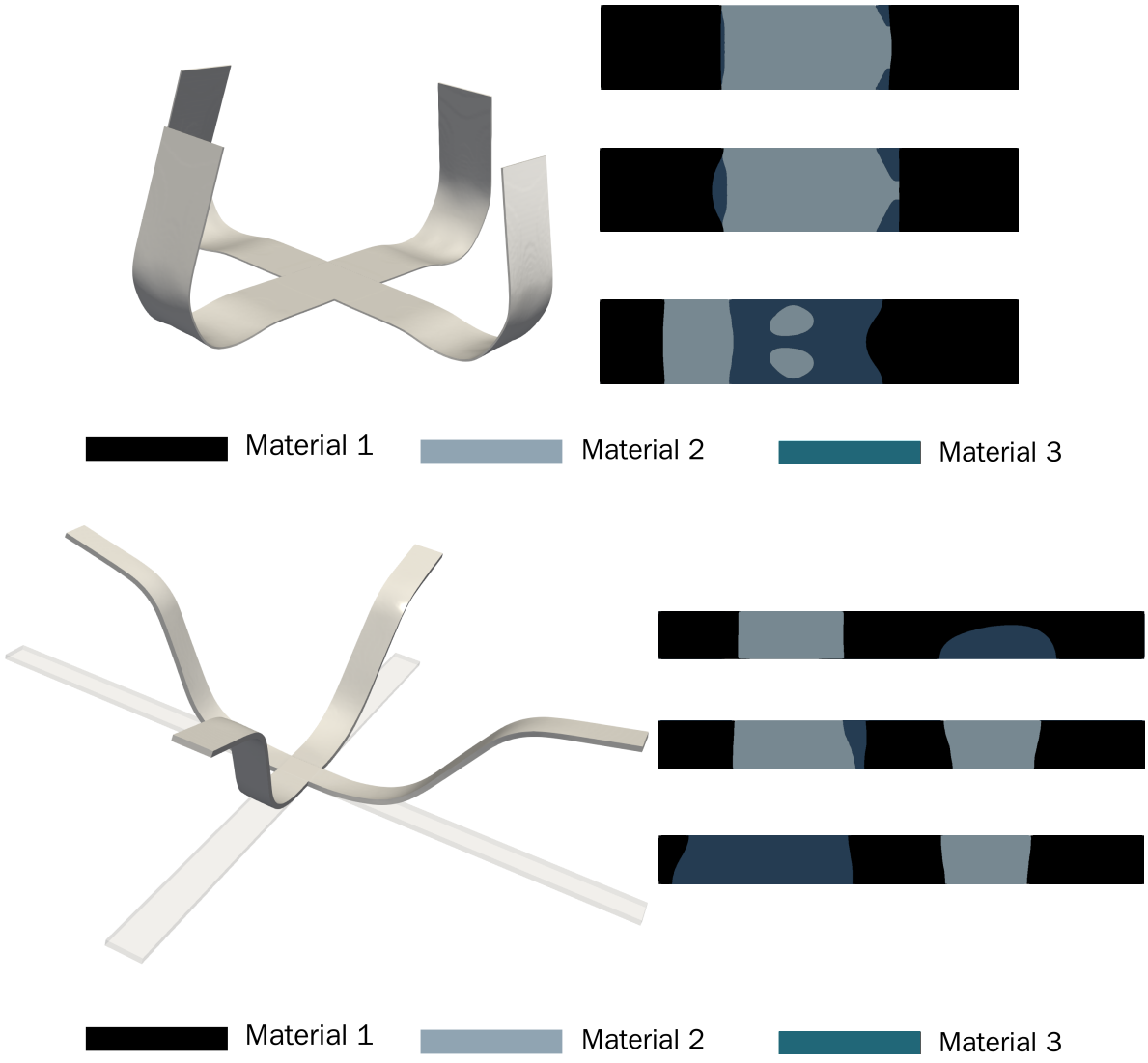

Figure 9: Example 2. *Top:* electrically induced deformation for optimal result corresponding with **actuation mode 1**, characterised by distribution of *Material 1*, *Material 2* and *Material 3* shown at each of the three layers. *Bottom:* electrically induced deformation for optimal result corresponding with **actuation mode 2**, characterised by distribution of *Material 1*, *Material 2* and *Material 3* shown at each of the three layers. In both designs, a composition is shown were three additional devices are placed at 90, 180 and 270 degrees with respect to the optimal design, in order to illustrate the gripping possibilities of the resulting device.

Figure 9_a shows the result of the topology optimisation algorithm for the objective function corresponding with **actuation mode 1**. Specifically, the regions where *Material 1, Material 2* and *Material 3* need to be placed at each of the three layers across the thickness are shown. Notice that these regions can be inferred from the values of the phase-field functions $\{\psi_1(\boldsymbol{X}), \psi_2(\boldsymbol{X})\}$ according to equation (27). In addition, the electrically induced deformation attained after the application of a voltage difference of value $\Delta\varphi = 1250$ (V) is also displayed in Figure 9_a. Clearly, the final shape of the electrically deformed DE design is in agreement with the target configuration in equation (56b).

On the other hand, Figure 9_b shows the result of the topology optimisation algorithm for the objective function corresponding with **actuation mode 2**, displaying the regions where *Material 1*, *Material 2* and *Material 3* need to be placed at each of the three layers across the thickness. In addition, the electrically induced deformation attained after the application of a voltage difference of value $\Delta\varphi = 5000$ (V) is also displayed in Figure 9_b. Clearly, the final shape of the electrically deformed DE design is in agreement with the target configuration in equation (56c).

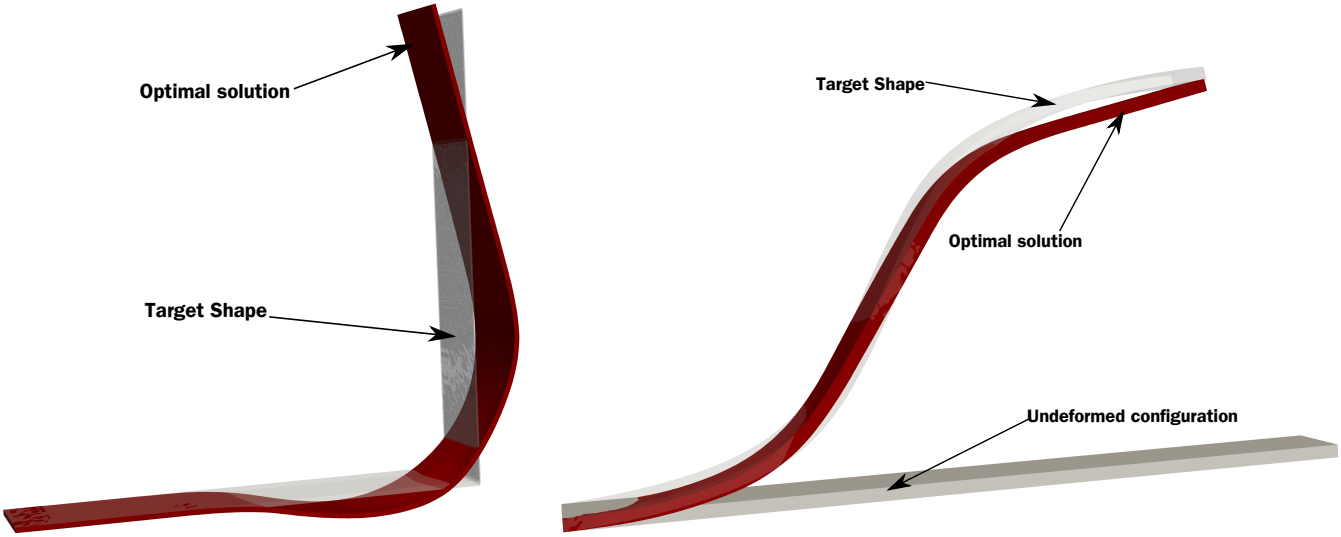

(a) (b)

Figure 10: Example 2. Target shape (trans-lucid) and optimal design (red colour) for the actuation modes in (56b) and (56c).

Figure 10 shows the comparison between the optimal solution provided by the topology optimisation algorithm and the target shape defined in both equations (56c) and (56b) for both actuation modes. As it can be observed, an absolutely perfect matching between both configurations might not be obtained. This is obvious in the case of **actuation mode 1**, where it is logical to guess that the corner features of the target configuration might be difficult to be perfectly reproduced by the optimal solution. Nonetheless, away from the corner, the overall agreement seems qualitatively reasonable. For **actuation mode 2**, although a perfect match is not obtained, the agreement between both configurations is more reasonable than in **actuation mode 1**.

4.3. Numerical example 3

In this example, the geometry depicted in Figure 11_a is considered. The initial seed for $\{\psi_1(\boldsymbol{X})|_{\tau=0}\,,\,\psi_2(\boldsymbol{X})|_{\tau=0}\}$ at the three layers across the thickness is shown in Figure 11_b (all layers are initialised in the same manner), where the red colour is associated with a value of $\psi_i(\boldsymbol{X})|_{\tau=0} = 1$, $i = \{1,2\}$ whilst the blue color is associated with $\psi_i(\boldsymbol{X})|_{\tau=0} = 0$, $i = \{1,2\}$. The Finite Element discretisation, yielding a total of 113400 nodes for both unknown fields $\{\boldsymbol{\phi}, \varphi\}$, is also shown in Figure 11.

Two different designs have been investigated for the DE layout described above. These correspond with two different actuation modes denoted as **actuation mode 1** and **actuation mode 2**. The target configuration $\boldsymbol{\phi}^\star$ for each of these actuation modes is described as

$$(\boldsymbol{\phi}^\star - \boldsymbol{X}) \cdot \boldsymbol{E}_3|_{\text{mode1}} = 0.2R_{\text{out}}\,(1 - \cos(2\theta))\,; \qquad (\boldsymbol{\phi}^\star - \boldsymbol{X}) \cdot \boldsymbol{E}_3|_{\text{mode2}} = 0.1R_{\text{out}}\,(1 - \cos(4\theta))\,, \tag{57}$$

where $\theta \in [0, 2\pi]$ parametrises in the circumferential direction the geometry in Figure 11.

Figure 12_a shows the result of the topology optimisation algorithm for the objective function corresponding with **actuation mode 1**. Specifically, the regions where *Material 1, Material 2* and *Material 3* need to be placed at each of the three layers across the thickness are shown. Notice that these regions can be inferred from the values of the phase-field functions $\{\psi_1(\boldsymbol{X}), \psi_2(\boldsymbol{X})\}$ according to equation (27). In addition, the electrically induced deformation attained after the application of a voltage difference of value $\Delta\varphi = 1000$ (V) is also displayed in Figure 12_a. Clearly, the final shape of the electrically deformed DE design is in agreement with the target configuration in equation $(57)_a$.

On the other hand, Figure 12_b shows the result of the topology optimisation algorithm for the objective function corresponding with **actuation mode 2**, displaying the regions where *Material 1, Material 2* and *Material 3* need to be placed at each of the three layers across the thickness. In addition, the electrically induced deformation attained after the application of a voltage difference of value $\Delta\varphi = 1000$ (V) is also displayed in Figure 12_b. Clearly, the final shape of the electrically deformed DE design is in agreement with the target configuration in equation $(57)_b$.

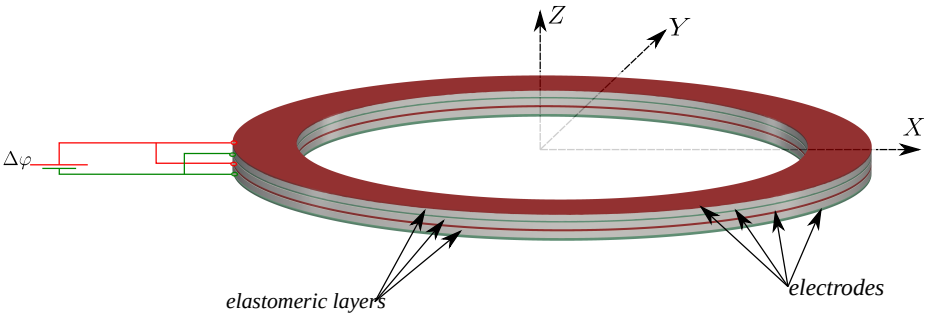

(a)

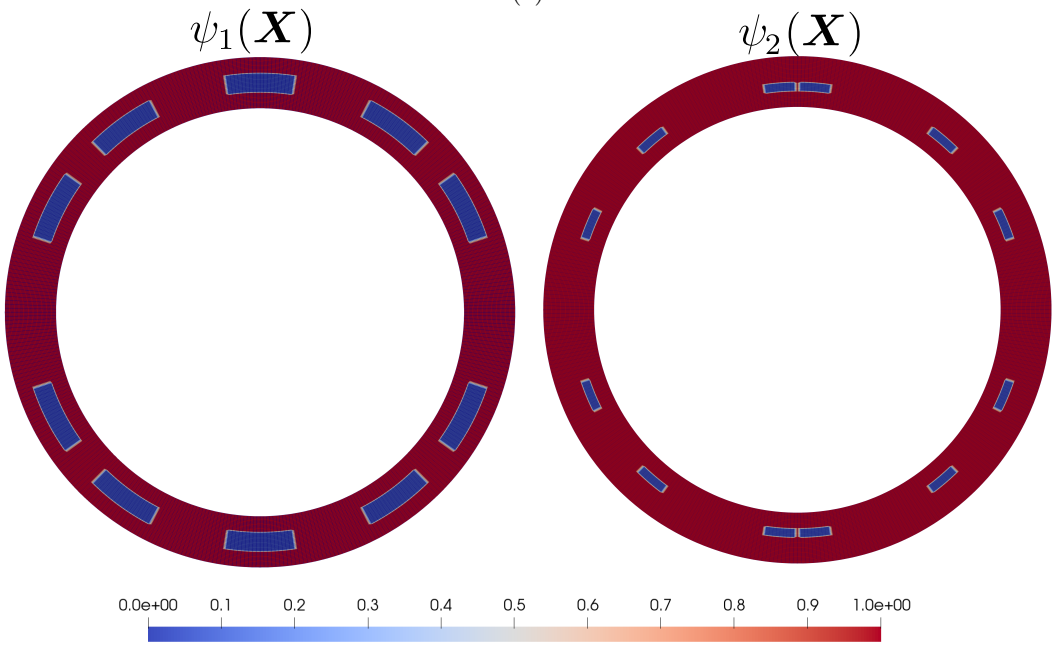

(b)

Figure 11: Example 1. (a) Geometry of the DE with outer and inner radius of $R_{\text{out}} = 0.05$ (m) and $R_{\text{in}} = 0.04$ (m), and with thickness of $h = R_{\text{out}}/180$ (m); (b) Common initial seed for the two phase-field functions $\{\psi_1(\boldsymbol{X}), \psi_2(\boldsymbol{X})\}$ for the three layers across the thickness.

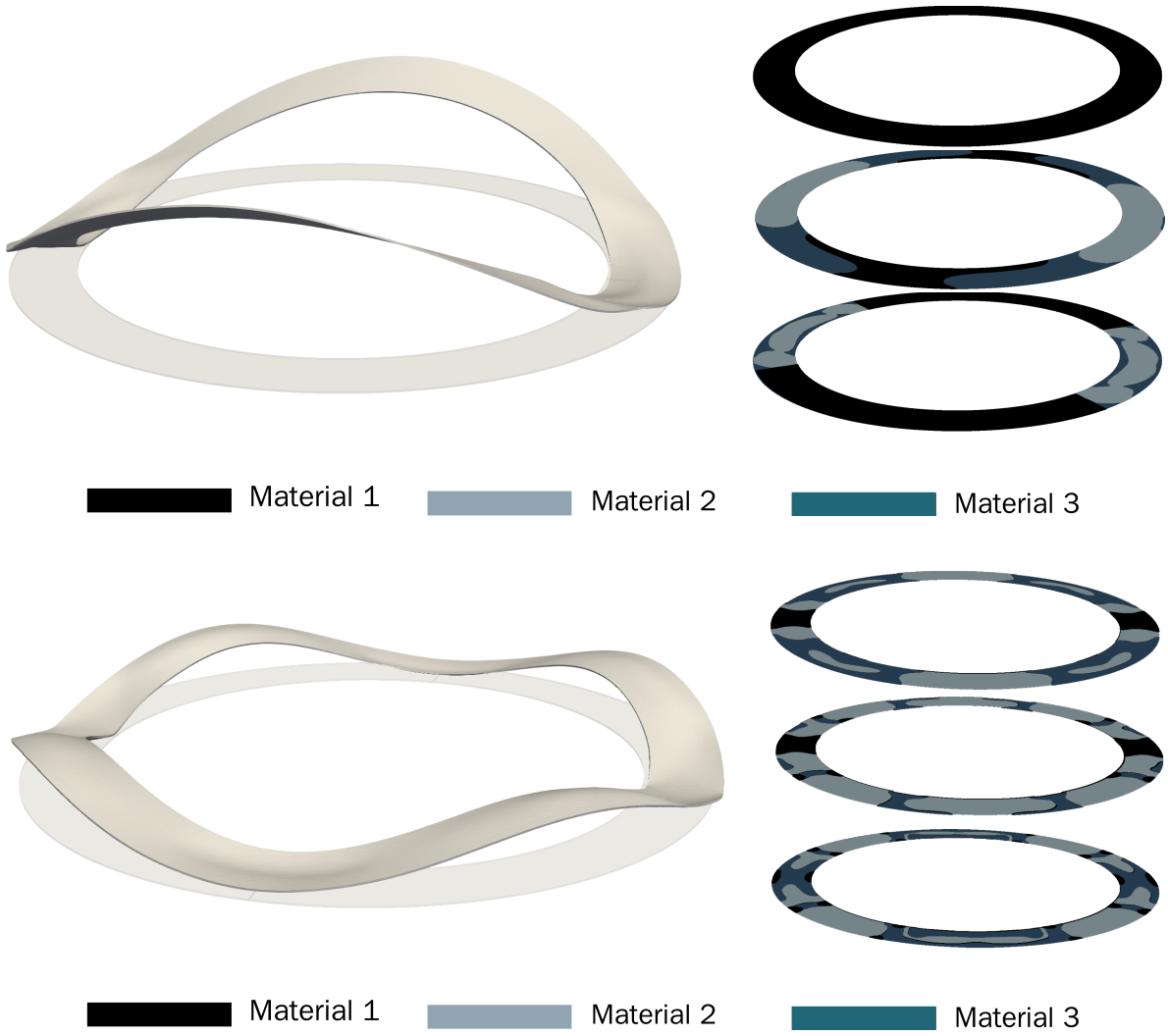

Figure 12: Example 1. *Top:* electrically induced deformation for optimal result corresponding with **actuation mode 1**, characterised by distribution of *Material 1*, *Material 2* and *Material 3* shown at each of the three layers. *Bottom:* electrically induced deformation for optimal result corresponding with **actuation mode 2**, characterised by distribution of *Material 1*, *Material 2* and *Material 3* shown at each of the three layers

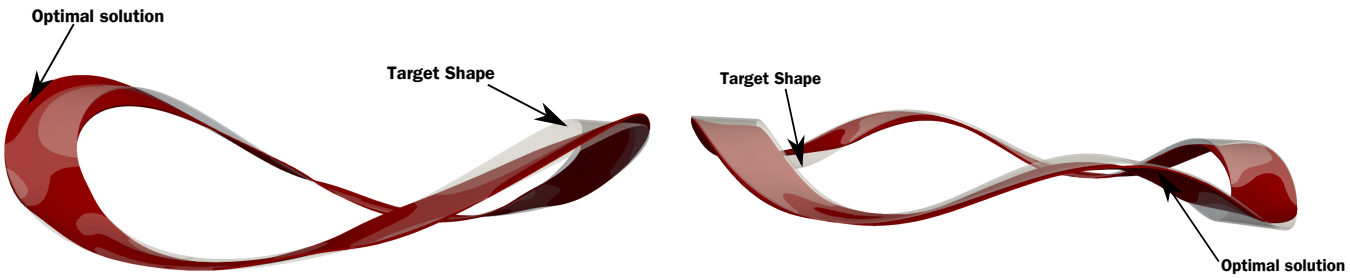

(a) (b)

Figure 13: Example 3. Target shape (trans-lucid) and optimal solutions (red colour) for both actuation modes in $(57)_a$ and $(57)_b$.

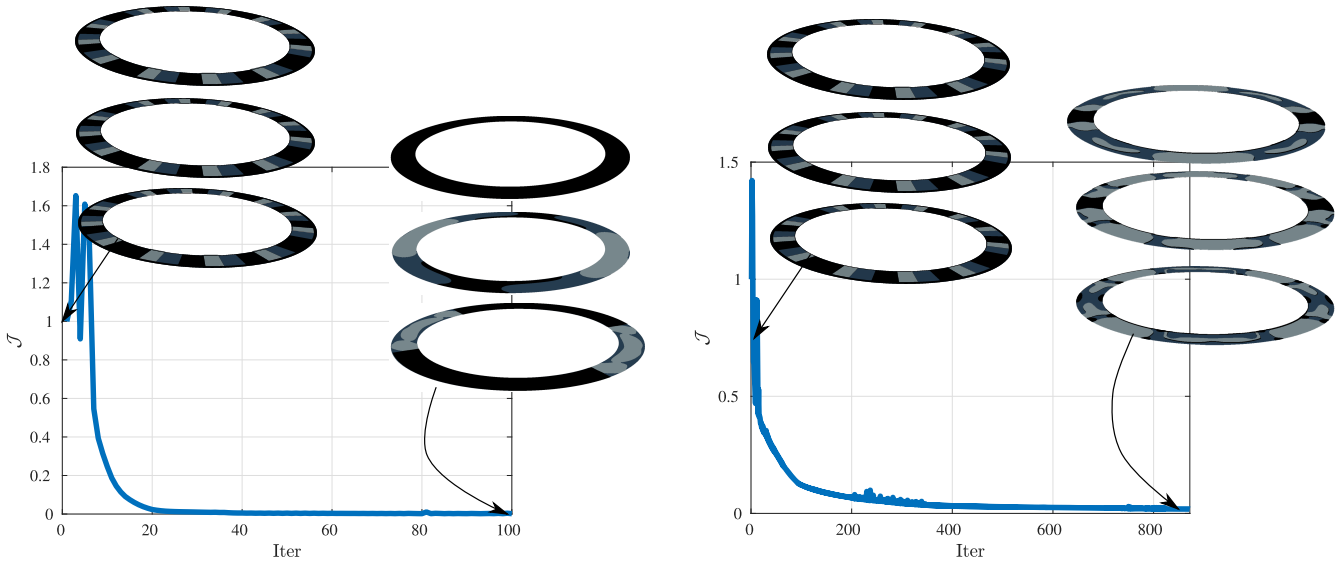

(a) (b)

Figure 14: Example 3. Evolution of the objective function $\mathcal{J}(\phi)$ associated with the target configuration for **actuation mode 1** and **actuation mode 2** in equations $(57)_a$ and $(57)_b$. $\mathcal{J}$ has been scaled with respect to its initial value at iteration 1. Distribution of *Material 1*, *Material 2* and *Material 3* at the initial topology optimisation iteration and the end of it (converged design).

Figure 13 shows the comparison between the optimal solution provided by the topology optimisation algorithm and the target shape defined in both equations $(57)_a$ and $(57)_b$ for both actuation modes. As it can be observed, the agreement between the optimisation-driven result and the target configuration is very good although not perfect. Finally, Figure 14 displays the smooth evolution of the respective objective functions $\mathcal{J}$ for both **actuation mode 1** and **actuation mode 2**.

5. Conclusions

This work has presented a novel engineering strategy for the design of DE-based actuators, capable of attaining complex electrically induced shape morphing configurations. In this approach, a multilayered DE prototype, interleaved with compliant electrodes spreading over the entire faces of the DE, has been considered. Efficient combination of several DE materials, characterised by different material properties, within each of the multiple layers of the device has been sought. Crucially, the resulting layout allows for the generation of heterogeneous electric fields within the device due to the spatial variation of the material properties within the layers and across them.

A novel computational framework has been developed in order to facilitate the design of new prototypes capable of attaining predefined electrically induced target configurations. The crucial ingredient of the proposed methodology lies on the development of a novel phase-field driven multi-material topology optimisation framework allowing for the consideration of several DE materials with different material properties, favouring the development of heterogeneous electric fields within the prototype. Although the numerical examples analysed have considered the combination of three different DE materials, the proposed multi-material framework can be generalised in order to handle an arbitrary number of different N DE materials. This can be done by means of the consideration of $N-1$ phase-field functions, evolving independently over the different layers across the thickness of the device through $N-1$ Allen-Cahn type evolution equations per layer.

A series of challenging proof-of-concept numerical examples has been included in order to assess the applicability of the proposed methodology. In all the examples, the final optimal designs permit to interpret, from the values of the $N-1$ phase-field functions, the topology of the regions where the N different DE materials must be conveniently placed in order to accomplish the underlying shape morphing objective.

Acknowledgements

The first author acknowledges the financial support of Fundación Séneca, through the contract with reference number 21132/SF/19 under the programe Subprograma Regional "Saavedra Fajardo de incorporación de doctores a Universidades y Centros de investigación de la Región de Murcia". First and second authors acknowledge the support provided by the Autonomous Community of the Region of Murcia, Spain through the programme for the development of scientific and technical research by competitive groups (20911/PI/18), included in the Regional Program for the Promotion of Scientific and Technical Research of Fundación Séneca - Agencia de Ciencia y

Tecnología de la Región de Murcia. The third author acknowledges the financial support received through the European Training Network Protechtion (Project ID: 764636) and of the UK Defence, Science and Technology Laboratory.

Appendix A. Finite Element spatial semi-discretisation

The various fields $\boldsymbol{\mathcal{Y}} = \{\boldsymbol{\phi}, \varphi, \boldsymbol{p}_{\boldsymbol{\phi}}, p_\varphi, \psi_1, \psi_2, \dots, \psi_{N-1}\}$ are interpolated using Finite Element discretisations as

$$\boldsymbol{\phi} \approx \sum_{a=1}^{n_{\boldsymbol{\phi}}} N_a^{\boldsymbol{\phi}} \boldsymbol{\phi}^a; \quad \varphi \approx \sum_{a=1}^{n_\varphi} N_a^{\varphi} \varphi^a; \quad \boldsymbol{p}_{\boldsymbol{\phi}} \approx \sum_{a=1}^{n_{\boldsymbol{\phi}}} N_a^{\boldsymbol{\phi}} \boldsymbol{p}_{\boldsymbol{\phi}}^a; \quad p_\varphi \approx \sum_{a=1}^{n_\varphi} N_a^{\varphi} p_\varphi^a; \quad \psi_i \approx \sum_{a=1}^{n_{\psi_i}} N_a^{\psi_i} \psi_i^a, \ i = \{1, 2, \dots, N-1\}, \tag{A.1}$$

where $N_a^{\boldsymbol{\mathcal{Y}}}$ correspond with the nodal shape function associated with the field $\boldsymbol{\mathcal{Y}}$ and node a of the discretisation. Furthermore, $n_{\boldsymbol{\mathcal{Y}}}$ denotes the number of nodes associated with discretisation of field $\boldsymbol{\mathcal{Y}}$, and $\boldsymbol{\mathcal{Y}}^a$ is the nodal value of the field $\boldsymbol{\mathcal{Y}}$. Moreover, N represents the total number of different DE materials combined to achieve a desired target configuration. Following a Bubnov-Galerkin type approach, identical discretisation is used for the corresponding virtual fields $\delta\boldsymbol{\mathcal{Y}}$. Finally, the same spatial discretisation is also used for corresponding unknown fields and adjoint states.

Appendix A.1. Spatial discretisation of the optimality conditions with respect to the adjoint states

The two optimality conditions in equation (43), for the specific case where $N = 2$ different DE materials are considered, can be spatially discretised as

$$D\Pi(\psi_1, \psi_2, \boldsymbol{\phi}, \varphi)[\delta \boldsymbol{p}_{\boldsymbol{\phi}}] = \sum_{a=1}^{n_{\boldsymbol{\phi}}} \delta \boldsymbol{p}_{\boldsymbol{\phi}}^a \cdot \boldsymbol{R}_a^{\boldsymbol{p}_{\boldsymbol{\phi}}} = 0; \qquad D\Pi(\psi_1, \psi_2, \boldsymbol{\phi}, \varphi)[\delta p_\varphi] = \sum_{a=1}^{n_\varphi} \delta p_\varphi^a R_a^{p_\varphi} = 0, \tag{A.2}$$

where the nodal residual components $\boldsymbol{R}_a^{\boldsymbol{p}_{\boldsymbol{\phi}}}$ and $R_a^{p_\varphi}$ are given by

$$\begin{aligned} \boldsymbol{R}_a^{\boldsymbol{p}_{\boldsymbol{\phi}}} &= \int_{\mathcal{B}_0} \boldsymbol{P}\left(\psi_1, \psi_2, \boldsymbol{F}, \boldsymbol{E}_0\right) \boldsymbol{\nabla}_0 N_a^{\boldsymbol{\phi}} \, dV - \int_{\mathcal{B}_0} \boldsymbol{f} N_a^{\boldsymbol{\phi}} \, dV - \int_{\partial_{\boldsymbol{t}}\mathcal{B}_0} \boldsymbol{t}_0 N_a^{\boldsymbol{\phi}} \, dA; \\ R_a^{p_\varphi} &= \int_{\mathcal{B}_0} \boldsymbol{D}_0\left(\psi_1, \psi_2, \boldsymbol{F}, \boldsymbol{E}_0\right) \cdot \boldsymbol{\nabla}_0 N_a^{\varphi} \, dV + \int_{\mathcal{B}_0} \rho_0 N_a^{\varphi} \, dV + \int_{\partial_\omega \mathcal{B}_0} \omega_0 N_a^{\varphi} \, dA, \end{aligned} \tag{A.3}$$

with $\boldsymbol{P}\left(\psi_1, \psi_2, \boldsymbol{F}, \boldsymbol{E}_0\right)$ and $\boldsymbol{D}_0\left(\psi_1, \psi_2, \boldsymbol{F}, \boldsymbol{E}_0\right)$ defined according to equation (32). Solution of the discrete nonlinear optimality conditions (A.2) is carried out via the Newton-Raphson iterative strategy (23), yielding the discrete counterparts of equation (25), i.e.

$$\begin{aligned} D^2\Pi(\psi_1, \psi_2, \boldsymbol{\phi}, \varphi)[\delta \boldsymbol{p}_{\boldsymbol{\phi}}; \Delta\boldsymbol{\phi}] &= \sum_{a=1}^{n_{\boldsymbol{\phi}}} \sum_{b=1}^{n_{\boldsymbol{\phi}}} \delta \boldsymbol{p}_{\boldsymbol{\phi}}^a \cdot \boldsymbol{K}_{ab}^{\boldsymbol{\phi}\boldsymbol{\phi}} \Delta\boldsymbol{\phi}^b; \qquad D^2\Pi(\psi_1, \psi_2, \boldsymbol{\phi}, \varphi)[\delta \boldsymbol{p}_{\boldsymbol{\phi}}; \Delta\varphi] = \sum_{a=1}^{n_{\boldsymbol{\phi}}} \sum_{b=1}^{n_\varphi} \delta \boldsymbol{p}_{\boldsymbol{\phi}}^a \cdot \boldsymbol{K}_{ab}^{\boldsymbol{\phi}\varphi} \Delta\varphi^b; \\ D^2\Pi(\psi_1, \psi_2, , \boldsymbol{\phi}, \varphi)[\delta p_\varphi; \Delta\boldsymbol{\phi}] &= \sum_{a=1}^{n_\varphi} \sum_{b=1}^{n_{\boldsymbol{\phi}}} \delta p_\varphi^a \left(\boldsymbol{K}_{ba}^{\boldsymbol{\phi}\varphi}\right)^T \Delta\boldsymbol{\phi}^b; \qquad D^2\Pi(\psi_1, \psi_2, \boldsymbol{\phi}, \varphi)[\delta p_\varphi; \Delta\varphi] = \sum_{a=1}^{n_\varphi} \sum_{b=1}^{n_\varphi} \delta p_\varphi^a K_{ab}^{\varphi\varphi} \Delta\varphi^b, \end{aligned} \tag{A.4}$$

where $\{\boldsymbol{\phi}^b, \varphi^b\}$ represent the nodal unknowns, with the stiffness tangent contributions $\boldsymbol{K}_{ab}^{\boldsymbol{\phi}\boldsymbol{\phi}}$, $\boldsymbol{K}_{ab}^{\boldsymbol{\phi}\varphi}$ and $\boldsymbol{K}_{ab}^{\varphi\varphi}$ expressed as

$$\begin{aligned} \left(\boldsymbol{K}_{ab}^{\boldsymbol{\phi}\boldsymbol{\phi}}\right)_{ij} &= \int_{\mathcal{B}_0} \left(\boldsymbol{\nabla}_0 N_a^{\boldsymbol{\phi}}\right)_I \left(\boldsymbol{\mathcal{C}}\left(\psi_1, \psi_2, \boldsymbol{F}, \boldsymbol{E}_0\right)\right)_{iIjJ} \left(\boldsymbol{\nabla}_0 N_b^{\boldsymbol{\phi}}\right)_J dV; \\ \left(\boldsymbol{K}_{ab}^{\boldsymbol{\phi}\varphi}\right)_i &= \int_{\mathcal{B}_0} \left(\boldsymbol{\nabla}_0 N_a^{\boldsymbol{\phi}}\right)_I \left(\boldsymbol{\mathcal{P}}^T\left(\psi_1, \psi_2, \boldsymbol{F}, \boldsymbol{E}_0\right)\right)_{iIJ} \left(\boldsymbol{\nabla}_0 N_b^{\varphi}\right)_J \, dV; \\ K_{ab}^{\varphi\varphi} &= -\int_{\mathcal{B}_0} \boldsymbol{\nabla}_0 N_a^{\varphi} \cdot \boldsymbol{\varepsilon}\left(\psi_1, \psi_2, \boldsymbol{F}, \boldsymbol{E}_0\right) \boldsymbol{\nabla}_0 N_b^{\varphi} \, dV, \end{aligned} \tag{A.5}$$

with $\{\boldsymbol{\mathcal{C}}, \boldsymbol{\mathcal{P}}, \boldsymbol{\varepsilon}\}$ defined according to (34).

Appendix A.2. Spatial discretisation of the optimality conditions with respect to the unknown fields

Discretisation of the optimality conditions (44) yields the following linear system of equations,

$$D\mathcal{L}(\psi_1, \psi_2, \boldsymbol{\phi}, \varphi, \boldsymbol{p}_{\boldsymbol{\phi}}, p_\varphi)[\delta\boldsymbol{\phi}] = -\sum_{a=1}^{n_{\boldsymbol{\phi}}} \sum_{b=1}^{n_{\boldsymbol{\phi}}} \delta\boldsymbol{\phi}^a \cdot \boldsymbol{K}_{ab}^{\boldsymbol{\phi}\boldsymbol{\phi}} \boldsymbol{p}_{\boldsymbol{\phi}}^b - \sum_{a=1}^{n_{\boldsymbol{\phi}}} \sum_{b=1}^{n_\varphi} \delta\boldsymbol{\phi}^a \cdot \boldsymbol{K}_{ab}^{\boldsymbol{\phi}\varphi} p_\varphi^b + \sum_{a=1}^{n_{\boldsymbol{\phi}}} \delta\boldsymbol{\phi}_a \cdot \boldsymbol{R}_a^{\mathcal{J}} = 0; \tag{A.6a}$$

$$D\mathcal{L}(\psi_1, \psi_2, \boldsymbol{\phi}, \varphi, \boldsymbol{p}_{\boldsymbol{\phi}}, p_\varphi)[\delta\varphi] = -\sum_{a=1}^{n_\varphi} \sum_{b=1}^{n_{\boldsymbol{\phi}}} \delta\varphi^a \left(\boldsymbol{K}_{ba}^{\boldsymbol{\phi}\varphi}\right)^T \boldsymbol{p}_{\boldsymbol{\phi}}^b - \sum_{a=1}^{n_\varphi} \sum_{b=1}^{n_\varphi} \delta\varphi^a K_{ab}^{\varphi\varphi} p_\varphi^b = 0, \tag{A.6b}$$

where $\{\boldsymbol{p}_{\boldsymbol{\phi}}^b, p_{\varphi}^b\}$ represent the nodal unknown fields. In addition, for the objective function in (40), the residual vector $\boldsymbol{R}_a^{\mathcal{J}}$ corresponding to the discretisation of $D\mathcal{J}(\boldsymbol{\phi})[\delta\boldsymbol{\phi}]$ yields

$$\boldsymbol{R}_a^{\mathcal{J}} = \int_D (\boldsymbol{\phi} - \boldsymbol{\phi}^*)\, N_b^{\boldsymbol{\phi}}\, dV. \tag{A.7}$$

Appendix A.3. Computation of the sensitivity and evolution of the phase field equation

The spatial discretisation of the phase field evolution equation (52) yields

$$\sum_{a=1}^{n_{\psi_i}} \sum_{b=1}^{n_{\psi_i}} \delta\psi_i^a K_{ab}^{\psi_i\psi_i} \Delta\psi_i^b = \sum_{a=1}^{n_{\psi_i}} \delta\psi_i^a R_a^{\psi_i}; \qquad i = \{1, 2\}, \tag{A.8}$$

where the stiffness matrix component $K_{ab}^{\psi_i\psi_i}$ and the residual component $R_a^{\psi_i}$ are expressed as

$$\begin{aligned} K_{ab}^{\psi_i\psi_i} &= \int_{\mathcal{B}_0} \left(\frac{1}{\Delta\tau} N_{\psi_i}^a N_{\psi_i}^b + \kappa \boldsymbol{\nabla}_0 N_{\psi_i}^a \cdot \boldsymbol{\nabla}_0 N_{\psi_i}^b + N_{\psi_i}^a N_{\psi_i}^b P(\psi_i^n) r(\boldsymbol{X}, \psi_i^n) \right) dV; \\ R_a^{\psi_i} &= \int_{\mathcal{B}_0} \left(\frac{\psi_i^n}{\Delta\tau} + Q(\psi_i^n) r(\boldsymbol{X}, \psi_i^n) \right) N_{\psi_i}^a\, dV, \end{aligned} \tag{A.9}$$

where

$$P(\psi_i^n) = \begin{cases} (\psi_i^n - 1); & \text{if } r(\boldsymbol{X}, \psi_i^n) \leq 0; \\ \psi_i^n; & \text{if } r(\boldsymbol{X}, \psi_i^n) > 0; \end{cases} \qquad Q(\psi_i^n) = \begin{cases} 0; & \text{if } r(\boldsymbol{X}, \psi_i^n) \leq 0; \\ \psi_i^n; & \text{if } r(\boldsymbol{X}, \psi_i^n) > 0. \end{cases} \tag{A.10}$$

For numerical reasons, the term $r(\boldsymbol{X}, \psi_n)$, whose expression is given in equation (51), is slightly modified, being defined as

$$r(\boldsymbol{X}, \psi_i) = \psi_i - \frac{1}{2} - 30\eta \widetilde{\mathcal{G}}_{\psi_i}(\boldsymbol{X}) \psi_i (1 - \psi_i); \qquad i = \{1, 2\}, \tag{A.11}$$

where $\widetilde{\mathcal{G}}_{\psi_1}$ are the dimensionless counterparts of $\mathcal{G}_{\psi_i}$ in (46), defined as

$$\widetilde{\mathcal{G}}_{\psi_i}(\boldsymbol{X}) = \frac{\mathcal{G}_{\psi_i}(\boldsymbol{X})}{||\boldsymbol{\mathcal{G}}_{\psi_i}||}, \tag{A.12}$$

where the vectors $\boldsymbol{\mathcal{G}}_{\psi_i}$ $(i = \{1, 2\})$ emanate from the Finite Element discretisation of $D\mathcal{L}[\Delta\psi_i]$ in (46), namely

$$\boldsymbol{\mathcal{G}}_{\psi_i} = \int_{\mathcal{B}_0} \mathcal{G}_{\psi_i}(\boldsymbol{X}) N_{\psi_i}^a\, dV; \qquad i = \{1, 2\}. \tag{A.13}$$

References

[1] R. Pelrine, R. Kornbluh, and J. Joseph. Electrostriction of polymer dielectrics with compliant electrodes as a means of actuation. *Sensors and Actuators A: Physical*, 64(1):77–85, 1998.

[2] R. Pelrine, R. Kornbluh, Q. Pei, and J. Joseph. High-speed electrically actuated elastomers with strain greater than 100 %. *Science*, 287(5454):836–839, 2000.

[3] G. Kofod, P. Sommer-Larsen, R. Kornbluh, and R. Pelrine. Actuation response of polyacrylate dielectric elastomers. *Journal of Intelligent Material Systems and Structures*, 14(12):787–793, 2003.

[4] A. L. Skov, O. Pei, D. Opris, R. J. Spontak, G. Gallone, H. Shea, and M. Y. Benslimane. *Dielectric Elastomers (DEs) as EAPs: Materials*, pages 1–28. Springer International Publishing, Cham, 2016.

[5] Kun Liu, Shitong Chen, Feifei Chen, and Xiangyang Zhu. A unidirectional soft dielectric elastomer actuator enabled by built-in honeycomb metastructures. *Polymers*, 12(3), 2020.

[6] T. Li, C. Keplinger, R. Baumgartner, S. Bauer, W. Yang, and Z. Suo. Giant voltage-induced deformation in dielectric elastomers near the verge of snap-through instability. *Journal of the Mechanics and Physics of Solids*, 61(2):611–628, 2013.

[7] B. Li, L. Liu, and Z. Suo. Extension limit, polarization saturation, and snap-through instability of dielectric elastomers. *International Journal of Smart and Nano Materials*, 2(2):59–67, 2011.

[8] R. Pelrine, R. Kornbluh, Q. Pei, S. Stanford, S. Oh, J. Eckerle, R. J. Full, M. A. Rosenthal, and K. Meijer. Dielectric elastomer artificial muscle actuators: toward biomimetic motion. In *Smart Structures and Materials 2002: Electroactive Polymer Actuators and Devices (EAPAD)*, volume 4695, pages 126–137. International Society for Optics and Photonics, SPIE, 2002.

[9] F. Chen and M. Y. Wang. Design optimization of soft robots: A review of the state of the art. *IEEE Robotics Automation Magazine*, 27(4):27–43, 2020.

[10] X. Zhao S. Yang and P. Sharma. Avoiding the pull-in instability of a dielectric elastomer film and the potential for increased actuation and energy harvesting. *Soft Matter*, 13:4552–4558, 2017.

[11] L. Chen, X. Yang, B. Wang, S. Yang, K. Dayal, and P. Sharma. The interplay between symmetry-breaking and symmetry-preserving bifurcations in soft dielectric films and the emergence of giant electro-actuation. *Extreme Mechanics Letters*, 43:101151, 2021.

[12] A. O'Halloran, F. O'Malley, and P. McHugh. A review on dielectric elastomer actuators, technology, applications, and challenges. *Journal of Applied Physics*, 104(7):071101, 2008.

[13] R. Poya, A. J. Gil, R. Ortigosa, R. Sevilla, J. Bonet, and W. A. Wall. A curvilinear high order finite element framework for electromechanics: From linearised electro-elasticity to massively deformable dielectric elastomers. *Computer Methods in Applied Mechanics and Engineering*, 329:75–117, 2018.

[14] J. Zhou, W. Hong, X. Zhao, Z. Zhang, and Z. Suo. Propagation of instability in dielectric elastomers. *International Journal of Solids and Structures*, 45(13):3739–3750, 2008.

[15] Samuel Shian, Roger M. Diebold, and David R. Clarke. Tunable lenses using transparent dielectric elastomer actuators. *Opt. Express*, 21(7):8669–8676, 2013.

[16] Suntak Park, Bongje Park, Saekwang Nam, Sungryul Yun, Seung Koo Park, Seongcheol Mun, Jeong Mook Lim, Yeonghwa Ryu, Seok Ho Song, and Ki-Uk Kyung. Electrically tunable binary phase fresnel lens based on a dielectric elastomer actuator. *Opt. Express*, 25(20):23801–23808, Oct 2017.

[17] E. Hajiesmaili and D.R. Clarke. Reconfigurable shape-morphing dielectric elastomers using spatially varying electric fields. *Nature Communicationes*, 10(183):1–7, 2019.

[18] E. Hajiesmaili, E. Khare, J. Lewis A. Chortos, and D.R. Clarke. Voltage-controlled morphing of dielectric elastomer circular sheets into conical surfaces. *Extreme Mechanics Letters*, 30:1–8, 2019.

[19] J. Martínez-Frutos, R. Ortigosa, and A. J. Gil. In-silico design of electrode meso-architecture for shape morphing dielectric elastomers. *Journal of the Mechanics and Physics of Solids*, 157, 2021.

[20] R. Ortigosa and J. Martínez-Frutos. Topology optimisation of stiffeners layout for shape-morphing of dielectric elastomers. *Structural and Multidisciplinary Optimization*, 64:3681–3703, 2021.

[21] M.A. Skylar-Scott, J. Mueller, C.W. Visser, and J.A. Lewis. Voxelated soft matter via multimaterial multinozzle 3D printing. *Nature*, 575:330–335, 2019.

[22] H. Yuk, B. Lu, S. Lin, K. Qu, J. Xu, J. Luo, and X. Zhao. 3D printing of conducting polymers. *Nature Communications*, 1604, 2020.

[23] J. T. Muth, D. M. Vogt, R. L. Truby, Y. Menguc, D. B. Kolesky, R. J. Wood, and J. A. Lewis. Embedded 3D printing of strain sensors within highly stretchable elastomers. *Advanced Materials*, 26(36):6307–6312, 2014.

[24] Y. Kim, H. Yuk, R. Zhao, S. A. Chester, and X. Zhao. Printing ferromagnetic domains for untethered fast-transforming soft materials. *Nature*, 558:274–279, 2018.

[25] Y. Kim, H. Yuk, R. Zhao, S. A. Chester, and X. Zhao. Magnetically actuated reconfigurable metamaterials as conformal electromagnetic filters. *Advanced Intelligent Systems*, 4, 2022.

[26] M. A. Moreno-Mateos, J. Gonzalez-Rico, E. Nunez-Sardinha, C. Gomez-Cruz, M.L. Lopez-Donaire, S. Lucarini, A. Arias, A. Muñoz-Barrutia, D. Velasco, and D. Garcia-Gonzalez. Magneto-mechanical system to reproduce and quantify complex strain patterns in biological materials. *Applied Materials Today*, 27:101437, 2022.

[27] D. Garcia-Gonzalez, T. Ter-Yesayants, M.A. Moreno-Mateos, and M.L. Lopez-Donaire. Hard-magnetic phenomena enable autonomous self-healing elastomers. *Composites Part B: Engineering*, 248:110357, 2023.

[28] A. Dorfmann and R. W. Ogden. Nonlinear electroelasticity. *Acta Mechanica*, 174(3-4):167–183, 2005.

[29] A. Dorfmann and R.W. Ogden. Nonlinear electroelastic deformations. *Journal of Elasticity*, 82(2):99–127, 2006.

[30] R. Bustamante, A. Dorfmann, and R.W. Ogden. On electric body forces and Maxwell stresses in nonlinearly electroelastic solids. *International Journal of Engineering Science*, 47(11-12):1131–1141, 2009.

[31] R. Bustamante and J. Merodio. Constitutive structure in coupled non-linear electro-elasticity: Invariant descriptions and constitutive restrictions. *International Journal of Non-Linear Mechanics*, 46(10):1315 – 1323, 2011.

[32] D. K. Vu, P. Steinmann, and G. Possart. Numerical modelling of non-linear electroelasticity. *International Journal for Numerical Methods in Engineering*, 70(6):685–704, 2007.

[33] R. M. McMeeking and C. M. Landis. Electrostatic forces and stored energy for deformable dielectric materials. *Journal of Applied Mechanics*, 72(4):581–590, 2008.

[34] J. M. Ball. Convexity conditions and existence theorems in nonlinear elasticity. *Archive for Rational Mechanics and Analysis*, 63(4):337–403, 1976.

[35] J. Schröder and P. Neff. Invariant formulation of hyperelastic transverse isotropy based on polyconvex free energy functions. *International Journal of Solids and Structures*, 40:401–445, 2003.

[36] J. E. Marsden and T. J. R. Hughes. *Mathematical foundations of elasticity*. 1994.

[37] A. J. Gil and R. Ortigosa. A new framework for large strain electromechanics based on convex multivariable strain energies: variational formulation and material characterisation. *Computer Methods in Applied Mechanics and Engineering*, 302:293–328, 2016.

[38] M. P. Bendsøe and O. Sigmund. *Topology optimization*. Springer-Verlag, Berlin, 2003. ISBN 3-540-42992-1. Theory, methods and applications.

[39] M. Wang, X. Wang, and D. Guo. A level-set method for structural topology optimization. *Computer Methods in Applied Mechanics and Engineering*, 192:227–246, 2003.

[40] G. Allaire, F. Jouve, and Toader. A. Structural optimization using sensitivity analysis and a level-set method. *Journal of Computational Physics*, 194:363–393, 2004.

[41] M. Burger and R. Stainko. Phase-field relaxation of topology optimization with local stress constraints. *SIAM Journal on Control and Optimisation*, 192:147–1466, 2003.

[42] Akihiro Takezawa, Shinji Nishiwaki, and Mitsuru Kitamura. Shape and topology optimization based on the phase field method and sensitivity analysis. *Journal of Computational Physics*, 229(7):2697–2718, 2010.

[43] J. Sokolowski and A. Zochowski. On the topological derivative in shape optimization. *SIAM Journal on Control and Optimisation*, 37:1251–1272, 1999.

[44] D. J. Munk and G. P. Steven. Topology and shape optimization methods using evolutionary algorithms: a review. *Structural and Multidisciplinary Optimization*, 52:613–631, 2015.

[45] Z. Kang and X. Wang. Topology optimization of bending actuators with multilayer piezoelectric material. *Smart Materials and Structures*, 19(7):075018, 2010.

[46] S.S. Nanthakumar, Tom Lahmer, Xiaoying Zhuang, Harold S. Park, and Timon Rabczuk. Topology optimization of piezoelectric nanostructures. *Journal of the Mechanics and Physics of Solids*, 94:316 – 335, 2016.

[47] X. Zhang, A. Takezawa, and Z. Kang. Topology optimization of piezoelectric smart structures for minimum energy consumption under active control. *Structural and Multidisciplinary Optimization*, 58:185–199, 2018.

[48] M. Kögl and E. Silva. Topology optimization of smart structures: Design of piezoelectric plate and shell actuators. *Smart Materials and Structures*, 14:387–399, 2005.

[49] A. Donoso and J. Bellido. Systematic design of distributed piezoelectric modal sensors/actuators for rectangular plates by optimizing the polarization profile. *Structural and Multidisciplinary Optimization*, 38:347–356, 2009.

[50] A. Donoso, J. Bellido, and J. Chacón. Numerical and analytical method for the design of piezoelectric modal sensors/actuators for shell-type structures. *International Journal for Numerical Methods in Engineering*, 81: 1700–1712, 2009.

[51] J.L. Sánchez-Rojas, J Hernando, A Donoso, J. Bellido, T. Manzaneque, A. Ababneh, H. Seidel, and U. Schmid. Modal optimization and filtering in piezoelectric microplate resonators. *Journal of Micromechanics and Microengineering*, 20:055027, 2010.

[52] D. Ruiz, J. Bellido, A. Donoso, and J.L. Sanchez-Rojas. Design of in-plane piezoelectric sensors for static response by simultaneously optimizing the host structure and the electrode profile. *Structural and Multidisciplinary Optimization*, 48:1023–1026, 2013.

[53] D. Ruiz, J. Bellido, and A. Donoso. Design of piezoelectric modal filters by simultaneously optimizing the structure layout and the electrode profile. *Structural and Multidisciplinary Optimization*, 53:715–730, 2015.

[54] D. Ruiz, Alex Díaz-Molina, O. Sigmund, A. Donoso, J. Bellido, and J.L. Sánchez-Rojas. Optimal design of robust piezoelectric unimorph microgrippers. *Applied Mathematical Modelling*, 55:1–12, 2018.

[55] D. Ruiz and O. Sigmund. Optimal design of robust piezoelectric microgrippers undergoing large displacements. *Structural and Multidisciplinary Optimization*, 55:71–82, 2018.

[56] C. Lundgaard and O. Sigmund. A density-based topology optimization methodology for thermoelectric energy conversion problems. *Structural and Multidisciplinary Optimisation*, 57:1427–1442, 2018.

[57] C. Lundgaard and O. Sigmund. Design of segmented off-diagonal thermoelectric generators using topology optimization. *Applied Energy*, 236:950–960, 2019.

[58] C. Lundgaard and O. Sigmund. Design of segmented thermoelectric peltier coolers by topology optimization. *Applied Energy*, 239:1003–1013, 2019.

[59] N. Wang, H. Guo, B. Chen, and X. Zhang. Design of a rotary dielectric elastomer actuator using topology optimization method. In *2017 International Conference on Manipulation, Automation and Robotics at Small Scales (MARSS)*, pages 1–6, July 2017.

[60] E. Bortot, O. Amir, and G. Shmuel. Topology optimization of dielectric elastomers for wide tunable band gaps. *International Journal of Solids and Structures*, 143:262–273, 2018.

[61] R. Ortigosa, J. Martínez-Frutos, D. Ruiz, A. Donoso, and J. C. Bellido. Density-based topology optimisation considering nonlinear electromechanics. *Structural and Multidisciplinary Optimization*, 64:257–280, 2021.

[62] R. Ortigosa and J. Martínez-Frutos. Multi-resolution methods for the topology optimization of nonlinear electro-active polymers at large strains. *Computational Mechanics*, 68:271–293, 2021.

[63] J. Bonet, A. J. Gil, and R. D. Wood. *Nonlinear Continuum Mechanics for Finite Element Analysis: Statics*. Cambridge University Press, 2016.

[64] J. Bonet, A. J. Gil, and R. Ortigosa. A computational framework for polyconvex large strain elasticity. *Computer Methods in Applied Mechanics and Engineering*, 283:1061–1094, 2015.

[65] J. Bonet, A. J. Gil, and R. Ortigosa. On a tensor cross product based formulation of large strain solid mechanics. *International Journal of Solids and Structures*, 84:49–63, 2016.

[66] M. H. Siboni and P. P. Castañeda. Fiber-constrained, dielectric-elastomer composites: Finite-strain response and stability analysis. *Journal of the Mechanics and Physics of Solids*, 68(0):211–238, 2014.

[67] David L. Henann, Shawn A. Chester, and Katia Bertoldi. Modeling of dielectric elastomers: Design of actuators and energy harvesting devices. *Journal of the Mechanics and Physics of Solids*, 61(10):2047–2066, 2013.

[68] Victor Lefèvre and Oscar Lopez-Pamies. Nonlinear electroelastic deformations of dielectric elastomer composites: I—ideal elastic dielectrics. *Journal of the Mechanics and Physics of Solids*, 99:409–437, 2017.

[69] Morteza H. Siboni and Pedro Ponte Castañeda. Fiber-constrained dielectric elastomer composites: Finite deformation response and instabilities under non-aligned loadings. *International Journal of Solids and Structures*, 184:73–98, 2020. Physics and Mechanics of Random Structures: From Morphology to Material Properties.

[70] J. Schröder. Anisotropic polyconvex energies. In J. Schröder and P. Neff, editors, *Poly-, quasi- and rank-one convexity in Applied Mechanics, volume 516 of CISM Courses and Lectures*, volume 516 of CISM Courses and Lectures, pages 53–105. Springer-Verlag, 2010.

[71] H. Godaba, Z.Q. Zhang, U. Gupta, G.Ch. Foo, and J. Zhu. Instabilities in dielectric elastomers: buckling, wrinkling, and crumpling. *Soft Matter*, 15:7137–7144, 2019.

[72] R. Ortigosa, J. Martínez-Frutos, A. J. Gil, and D. Herrero-Pérez. A new stabilisation approach for level-set based topology optimisation of hyperelastic materials. *Structural and Multidisdiplinary Optimization*, 60: 2343–2371, 2019.

[73] R. Ortigosa and A. J. Gil. A new framework for large strain electromechanics based on convex multi-variable strain energies: Finite element discretisation and computational implementation. *Computer Methods in Applied Mechanics and Engineering*, 302:329–360, 2016.

[74] R. Ortigosa, A. J. Gil, and C. H. Lee. A computational framework for large strain nearly and truly incompressible electromecahnics based on convex multi-variable strain energies. *Computer Methods in Applied Mechanics and Engineering*, 310:297–334, 2016.